

## THE LOCAL ISM AND ITS INTERACTION WITH THE WINDS OF NEARBY LATE-TYPE STARS<sup>1</sup>

BRIAN E. WOOD<sup>2</sup> AND JEFFREY L. LINSKY

Joint Institute for Laboratory Astrophysics, University of Colorado, and National Institute of Standards and Technology,  
 Boulder, CO 80309-0440; woodb@marmot.colorado.edu, jlinsky@jila.colorado.edu

Received 1997 July 14; accepted 1997 August 21

### ABSTRACT

We present new Goddard High-Resolution Spectrograph (GHRS) observations of the Ly $\alpha$  and Mg II absorption lines seen toward the nearby stars 61 Cyg A and 40 Eri A. We use these data to measure interstellar properties along these lines of sight and to search for evidence of circumstellar hydrogen walls, which are produced by collisions between the stellar winds and the local interstellar medium (LISM). We were able to model the Ly $\alpha$  lines of both stars without hydrogen-wall absorption components, but for 61 Cyg A the fit required a stellar Ly $\alpha$  line profile with an improbably deep self-reversal, and for 40 Eri A the fit required a very low deuterium-to-hydrogen ratio that is inconsistent with previous GHRS measurements. Since these problems could be rectified simply by including stellar hydrogen-wall components with reasonable attributes, our preferred fits to the data include these components.

We have explored several ways in which the hydrogen-wall properties measured here and in previous work can be used to study stellar winds and the LISM. We argue that the existence of a hydrogen wall around 40 Eri A and a low H I column density along that line of sight imply that either the interstellar density must decrease toward 40 Eri A or the hydrogen ionization fraction ( $x$ ) must increase. We find that hydrogen-wall temperatures are larger for stars with faster velocities through the LISM. The observed temperature-velocity relation is consistent with the predictions of hydromagnetic shock jump conditions. More precise comparison of the data and the jump conditions suggests crude upper limits for both  $x$  and the ratio of magnetic to thermal pressure in the LISM ( $\alpha$ ):  $x < 0.6$  and  $\alpha < 2$ . The latter upper limit corresponds to a limit on the LISM magnetic field of  $B < 5 \mu\text{G}$ . These results imply that the plasma Mach number of the interstellar wind flowing into the heliosphere is  $M_A > 1.3$ , which indicates that the collision is supersonic and that there should therefore be a bow shock outside the heliopause in the upwind direction.

Finally, we estimate stellar wind pressures ( $P_{\text{wind}}$ ) from the measured hydrogen-wall column densities. These estimates represent the first empirical measurements of wind properties for late-type main-sequence stars. The wind pressures appear to be correlated with stellar X-ray surface fluxes,  $F_X$ , in a manner consistent with the relation  $P_{\text{wind}} \propto F_X^{-1/2}$ , a relation that is also consistent with the variations of  $P_{\text{wind}}$  and  $F_X$  observed during the solar activity cycle. If this relation can in fact be generalized to solar-like stars, as is suggested by our data, then it is possible to estimate stellar wind properties simply by measuring stellar X-rays. One implication of this is that stellar wind pressures and mass-loss rates are then predicted to increase with time, since  $F_X$  is known to decrease with stellar age.

*Subject headings:* ISM: general — stars: individual (61 Cygni A, 40 Eridani A) — stars: late-type — stars: mass loss — ultraviolet: ISM

### 1. INTRODUCTION

The interaction between the solar wind (SW) and the local interstellar medium (LISM) has been a subject of study for over four decades (see the review of Holzer 1989). This interaction determines the size of the heliosphere, which is the volume of space dominated by the SW. Models of the heliosphere generally predict the existence of three important discontinuities in the flows of the LISM and SW material. The termination shock is an oval-shaped boundary surrounding the Sun, where the supersonic SW is decelerated to subsonic speeds. Further out in the direction of the inflowing LISM material (i.e., in the “upwind” direction) lies the bow shock, where the supersonic inter-

stellar wind is decelerated to subsonic speeds. Finally, between these two shocks lies the heliopause, which separates the plasma flows of the solar and interstellar winds and defines the outer boundary of the heliosphere.

A problem that has always plagued studies of the heliosphere is the lack of observational constraints for the models. Properties of the SW and LISM particles in the solar system have been measured by *Ulysses* and the *Voyager* satellites, among others, but inferring properties of the heliosphere outside of the solar system from these data is difficult and somewhat model dependent. Uncertainties in heliospheric models are magnified by our incomplete knowledge of the properties of the ambient LISM. One consequence of these uncertainties is that the distances from the Sun to the termination shock, heliopause, and bow shock remain unknown. (In the upwind direction, the most recent models predict these three distances to be roughly 80, 120, and 250 AU, respectively.) Furthermore, the very existence of the bow shock remains somewhat in doubt (Zank et al. 1996; Gayley et al. 1997).

<sup>1</sup> Based on observations with the NASA/ESA *Hubble Space Telescope*, obtained at the Space Telescope Science Institute, which is operated by the Association of Universities for Research in Astronomy Inc., under NASA Contract NAS5-26555.

<sup>2</sup> Present address: Center for Astrophysics, 60 Garden Street, Cambridge, MA 02138.

Fortunately, a promising new technique for studying the outer heliosphere has recently been discovered using data from the *Hubble Space Telescope* (*HST*). Linsky & Wood (1996) observed the Ly $\alpha$  lines of the nearby stars  $\alpha$  Cen A and B using the Goddard High Resolution Spectrograph (GHRS) onboard *HST* to analyze the interstellar neutral hydrogen and deuterium absorption lines. However, they found that a second H I absorption component was necessary to fit the data in addition to the LISM component. In a fortuitous convergence of theory and observation, Linsky & Wood (1996) discovered that the most recent models of the heliosphere offered an attractive interpretation for this second component.

Initially, models of the heliosphere considered only plasma interactions between the fully ionized SW and the partially ionized LISM, but Holzer (1972) and Wallis (1975) demonstrated that the neutral atoms in the LISM could play an important role in the SW-LISM interaction through charge exchange processes. However, only very recently have models achieved the sophistication necessary to treat the ions and neutrals in a fully self-consistent manner (Baranov & Malama 1995; Pauls, Zank, & Williams 1995; Zank et al. 1996; Williams et al. 1997). One important prediction of these models is the existence of a region of heated, compressed, and decelerated H I located just outside of the heliopause. The predicted properties of this “hydrogen wall” (or “H wall” for short) agree very well with the H I column density, temperature, and velocity measured for the second H I absorption component seen toward  $\alpha$  Cen.

Gayley et al. (1997) presented a more direct comparison between the  $\alpha$  Cen data and the H I absorption predicted for that line of sight by the models, and they concluded that the solar H wall could indeed explain the non-LISM H I absorption detected by Linsky & Wood (1996). Another goal of their work was to assess the potential of the H-wall Ly $\alpha$  absorption for constraining the input parameters of the heliospheric models. They found that the  $\alpha$  Cen data were useful for this purpose. In particular, they tentatively concluded that models with an interstellar Mach number of  $M \approx 0.9$  best fit the data, which suggests that the bow shock is nonexistent and that a substantial amount of magnetic and/or cosmic-ray pressure must therefore be present in the LISM. Clearly, observations of other lines of sight are needed to further refine these analyses, and Williams et al. (1997) have discussed potentially useful targets.

The usefulness of the hydrogen-wall phenomenon does not end with studies of our heliosphere. Since the Sun has an H wall surrounding it, similar H walls might be expected around other Sun-like stars. Linsky & Wood (1996) considered the possibility that a hydrogen wall around  $\alpha$  Cen contributes to the H I absorption seen along that line of sight, and Gayley et al. (1997) concluded that this absorption is indeed probably present. A more convincing detection of a stellar hydrogen wall was provided by Wood, Alexander, & Linsky (1996), who discovered a non-LISM H I absorption component toward the nearby K5 V star  $\epsilon$  Ind with properties inconsistent with the solar H wall but consistent with a stellar H wall. Wood et al. (1996) also reported a more tentative detection of an H wall around the active binary system  $\lambda$  And (G8 IV–III + ?). Finally, Dring et al. (1997) found evidence for an H wall around the nearby K1 V star  $\epsilon$  Eri.

The potential importance of stellar H walls is threefold:

1. By observing what happens to the H walls when the properties of the LISM and/or stellar wind are changed, we can test our basic understanding of the interaction between a solar-like wind and the LISM.

2. Stellar H walls can potentially be used as probes for studying spatial variations of LISM properties, in a fashion analogous to that envisioned by Frisch (1993).

3. The stellar H walls may also be useful as diagnostics for the properties of stellar winds.

This last item is particularly important because currently the winds of solar-like stars are completely undetectable except through their interactions with the LISM. In fact, the detection of the  $\epsilon$  Ind H wall represents the first detection of a wind around a solar-like star. If properties of these winds can be inferred from the H-wall measurements, we could study for the first time how these properties vary with stellar activity, age, spectral type, and other parameters.

In this paper, we first attempt to detect H walls around two additional nearby stars using new GHRS observations. We then compile the properties of the stellar H walls detected so far and assess the usefulness of these data for studying the physics of “astrospheres” (a word analogous to “heliosphere”), the properties of the LISM, and the properties of solar-like stellar winds.

## 2. GHRS OBSERVATIONS OF 61 CYG A AND 40 ERI A

One of the reasons that the stellar H wall of  $\epsilon$  Ind proved to be detectable was the star’s high speed through the LISM ( $64.0 \text{ km s}^{-1}$ ; Wood et al. 1996). This large velocity produces a very hot H wall with a substantial deceleration of the incoming neutral hydrogen atoms. We therefore observe a very broad Ly $\alpha$  absorption profile that is partially separated from the LISM absorption. A large stellar velocity generally means a large line-of-sight radial velocity and a substantial wavelength difference between the stellar Ly $\alpha$  emission and the LISM Ly $\alpha$  absorption, which is very helpful in the analysis of the Ly $\alpha$  line for reasons that will become clear in § 4 (see also Wood et al. 1996). Thus, in our search for promising targets for stellar H-wall analyses, we chose to look only at stars moving with high speeds through the LISM. In particular, we selected stars that are moving rapidly toward us, so that we could observe the upwind portion of the H wall where it should be most visible. It was also important to select stars that are very nearby to minimize the amount of obscuring LISM absorption.

The observations presented in this paper are of 61 Cyg A (K5 V) and 40 Eri A (K1 V). The former (latter) is located at a distance of 3.5 (4.8) pc (Gliese & Jahreiss 1991), with a radial velocity of  $-64.5$  ( $-42.7$ )  $\text{km s}^{-1}$  (Beavers & Eitter 1986) and a speed through the LISM of  $85.0$  ( $123.2$ )  $\text{km s}^{-1}$ . In order to compute these velocities relative to the LISM, we used the known proper motions of the stars from Hirshfeld, Sinnott, & Ochsenbein (1991) in addition to the radial velocities and distances given above, and we also assumed that the local interstellar cloud (LIC) flow vector from Lallement et al. (1995) is applicable for the interstellar medium surrounding both 61 Cyg A and 40 Eri A. This should be a sensible assumption considering the close proximity of both stars, but we will show in § 3 that there is more than one velocity component toward 61 Cyg A, implying a different LISM flow vector for the 61 Cyg A vicinity. Multiple LISM components are seen toward many other nearby

stars (Linsky et al. 1995; Lallement et al. 1994, 1995), but these additional components are generally not widely separated from the LIC component—for 61 Cyg A the velocity difference is only about  $6 \text{ km s}^{-1}$ . Thus, we think the LIC flow vector should still be a reasonable approximation for the true vector.

Both 61 Cyg A and 40 Eri A are members of visual binary systems. The former has a K7 V companion located about 100 AU from the primary, and the latter has two companions: a white dwarf and an M4.5 V star, both about 400 AU from the primary. The existence of these companion stars could be very relevant to our analysis, if these stars (and their accompanying winds) are close enough to be located within the astrospheres of our target stars. For the Sun, the estimated upwind distance to the heliopause is about 120 AU, but we expect the astropause distances for 61 Cyg A and 40 Eri A to be much shorter because of the large velocities of these stars through the LISM—perhaps only about 30 AU (see § 5.3). Because this distance is significantly shorter than the distances from our target stars to their companions, we tentatively conclude that the companions to 61 Cyg A and 40 Eri A do not reside in the astrospheres of the primary stars and do not significantly influence the LISM–stellar wind interactions of 61 Cyg A and 40 Eri A, at least not in the upwind directions where our lines of sight are directed.

We observed 61 Cyg A and 40 Eri A with the GHRS on 1996 October 17 and 1997 January 28, respectively. The observations are summarized in Table 1. See Brandt et al. (1994) and Heap et al. (1995) for a full description of the GHRS and its capabilities. For each star, we observed the Mg II  $h$  and  $k$  lines (at 2802.705 and 2795.528 Å, respectively) with the echelle-B grating, and we then obtained a much longer exposure of the H I Ly $\alpha$  line at 1215.670 Å using the echelle-A grating. We used the FP-SPLIT mode for all of our observations to maximize the signal-to-noise ratio (S/N) of the data (Heap et al. 1995), and we obtained images of the platinum calibration lamp prior to each science exposure to maximize the accuracy of the wavelength calibrations. The spectral resolution was optimized by observing through the small science aperture (SSA). The CALHRS software prepared by the GHRS team was used to reduce the data (Robinson et al. 1992).

Figure 1 shows the Ly $\alpha$  observations, which are plotted on a velocity scale in the stellar rest frame. Broad, saturated interstellar H I absorption, centered at about  $60 \text{ km s}^{-1}$ , is seen superposed on the stellar emission line in both spectra. Narrower interstellar deuterium (D I) absorption is located at about  $-20 \text{ km s}^{-1}$ . Vertical dotted lines in the figure mark the expected locations of geocoronal H I emission/absorption. For 61 Cyg A, a weak geocoronal emission feature is seen precisely at the expected location, which speaks well for the accuracy of the wavelength calibration.

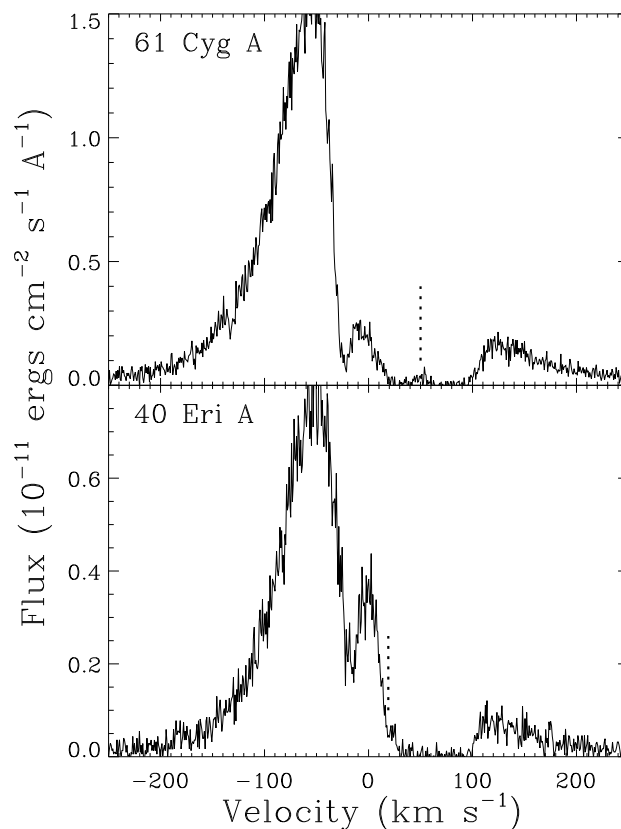


FIG. 1.—GHRS spectra of the Ly $\alpha$  lines of 61 Cyg A and 40 Eri A, plotted on a velocity scale in the stellar rest frames. Broad interstellar H I absorption is centered near  $60 \text{ km s}^{-1}$ , and narrower interstellar D I absorption is seen near  $-20 \text{ km s}^{-1}$ . The vertical dotted lines mark the locations of geocoronal emission, or absorption in the case of 40 Eri A.

We correct for this emission by subtracting a Gaussian fit to the feature from the data. For 40 Eri A, the dotted line does not lie within the core of the H I absorption but instead is located on the blue side of the absorption line. Thus, we see the geocoronal line in absorption rather than emission. This absorption is much harder to remove than the geocoronal emission seen toward 61 Cyg A. We found that it could be removed accurately only by including an extra absorption component in our fits to the entire Ly $\alpha$  profile. We will return to this issue in § 4.2.

### 3. ANALYSIS OF THE Mg II LINES

Our primary goal in this paper is to search for stellar H-wall absorption in the Ly $\alpha$  lines, but this absorption will be highly blended with the LISM H I absorption. We must therefore model the LISM absorption as accurately as possible. The narrow interstellar Mg II lines are very useful for this purpose, as they can be used to search for multiple

TABLE 1  
SUMMARY OF GHRS OBSERVATIONS

Target	Grating	Aperture	Spectral Range (Å)	Spectral Resolution ( $\text{km s}^{-1}$ )	Exposure Time (s)	Date	Start Time (UT)
61 Cyg A.....	Echelle-B	SSA	2790–2805	3.5	969	1996 Oct 17	5:33
	Echelle-A	SSA	1212–1219	3.5	4847	1996 Oct 17	7:01
40 Eri A.....	Echelle-B	SSA	2790–2805	3.5	862	1997 Jan 28	6:04
	Echelle-A	SSA	1212–1219	3.5	4847	1997 Jan 28	7:32

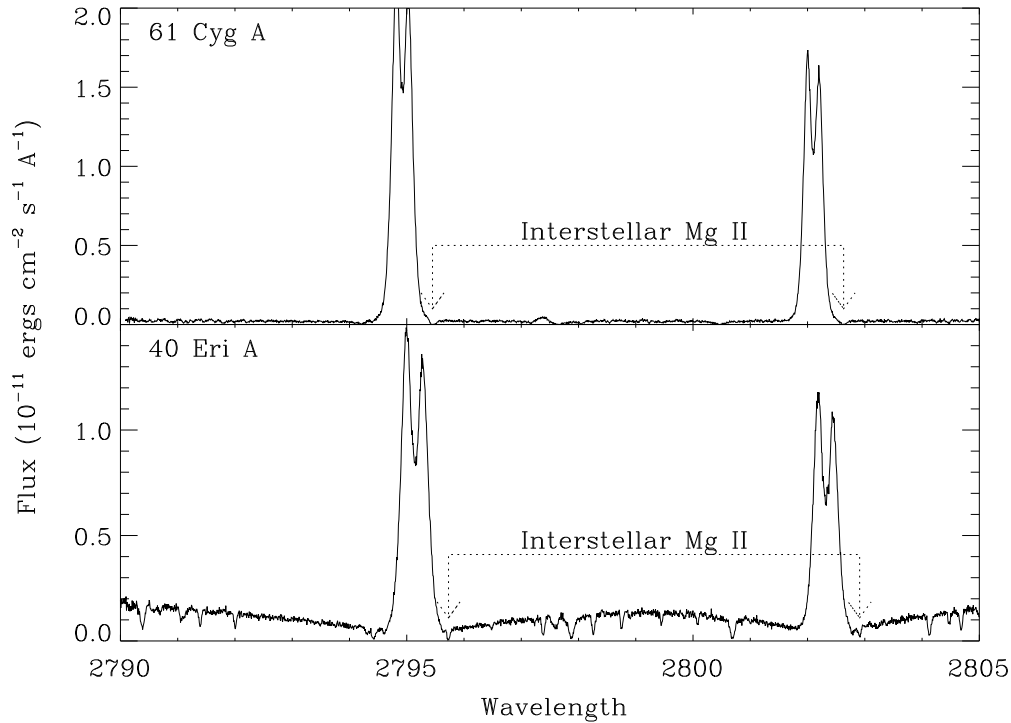


FIG. 2.—GHR spectra of the Mg II *h* and *k* lines at 2802 and 2795 Å, respectively, for both 61 Cyg A and 40 Eri A. Arrows mark the locations of interstellar Mg II absorption lines.

LISM components along each line of sight, components that would not be resolved in the broader H I and D I lines. Figure 2 displays the Mg II observations and indicates the locations of the interstellar absorption lines. Owing to the large negative radial velocities of 61 Cyg A and 40 Eri A, the absorption lines miss the stellar chromospheric emission lines entirely. Fortunately, there is sufficient background flux provided by the stellar UV continua that we can still detect and measure the LISM absorption, albeit with significantly less accuracy than if the absorption were superposed on the brighter emission lines.

In Figures 3 and 4, the LISM Mg II absorption is displayed on a heliocentric velocity scale. For the 61 Cyg A data, the *h* and *k* absorption profiles appear to be inconsistent, but we believe that this is due to a blended stellar absorption line located in the shaded region in Figure 3. A very weak stellar absorption feature is seen at this location in the spectrum of  $\alpha$  Cen B (Linsky & Wood 1996). This feature may also be present in the 40 Eri A spectrum (see Fig. 2), but it is not as apparent. The large width and asymmetric appearance of the Mg II lines seen toward 61 Cyg A indicates that more than one interstellar component must be present. We therefore fitted the lines with two components, as shown in Figure 3. Polynomial fits are used to estimate the stellar background continuum upon which the LISM absorption lines are superposed. We fit both Mg II lines simultaneously to constrain the fit as completely as possible, ignoring the shaded region. The best fit is defined as the one that minimizes  $\chi^2_\nu$  (Bevington & Robinson 1992).

The opacity profiles of the two components are modeled as Voigt functions. A correction is made for instrumental broadening, assuming a Gaussian instrumental profile with a width of 3.7 pixels (Gilliland 1994). The dotted lines in Figure 3 show the individual absorption components before instrumental broadening, and the thick solid lines show the

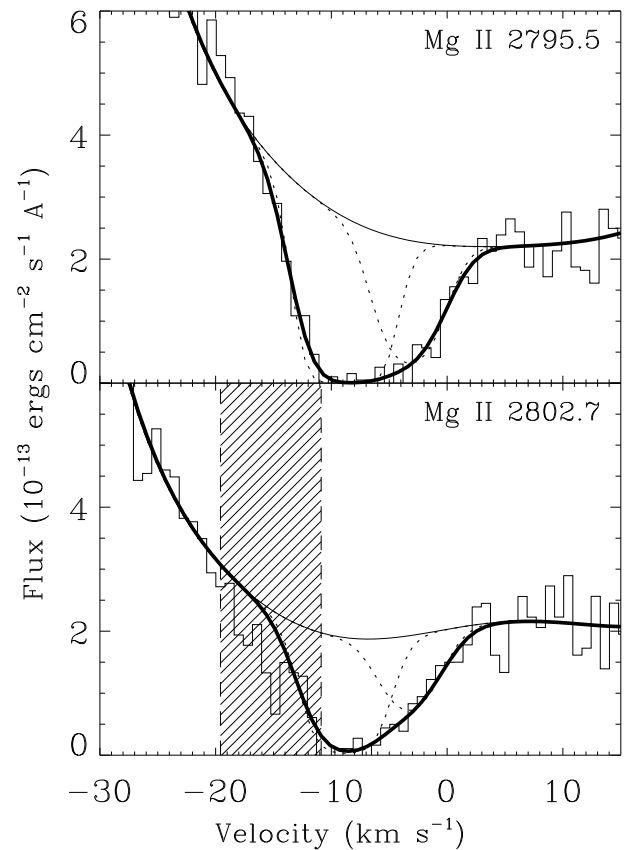


FIG. 3.—Two-component fits to the interstellar Mg II absorption lines seen toward 61 Cyg A, with the individual components shown as dotted lines and the combination of the two components shown as thick solid lines (after convolution with the instrumental profile). The shaded region was ignored in the fit due to contamination from a stellar absorption line. The data are plotted on a heliocentric velocity scale.

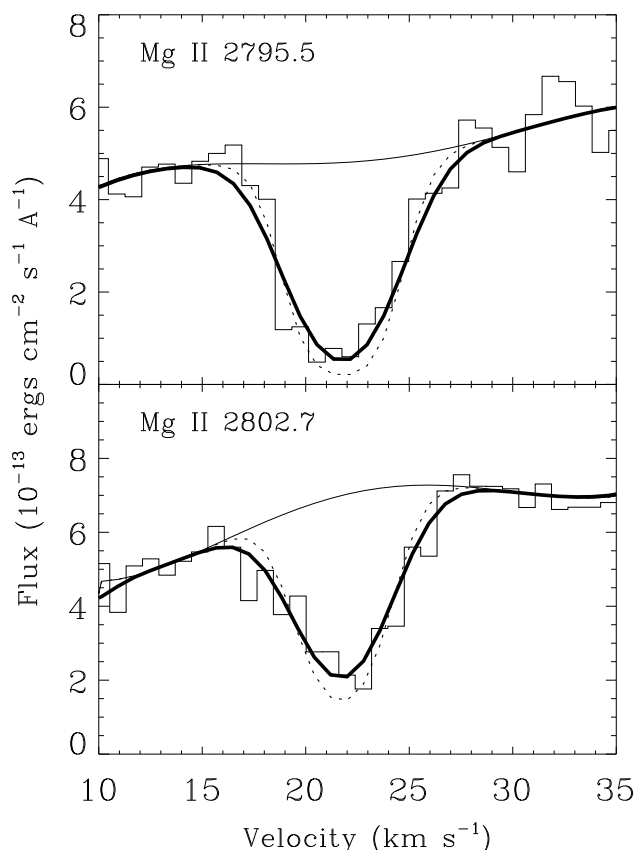


FIG. 4.—Single-component fits to the Mg II absorption lines seen toward 40 Eri A. The fitted components are shown both before (*dotted lines*) and after (*thick solid lines*) convolution with the instrumental profile. The data are plotted on a heliocentric velocity scale.

combination of the two components after instrumental broadening. The low S/N of the data and the highly blended nature of the two components prevent us from deriving a unique fit to the data without first reducing the number of free parameters. We address this problem by forcing both components to have the same Doppler parameter. The Doppler parameter ( $b$ ) of an absorption profile is related to the temperature ( $T$ ) and nonthermal velocity ( $\xi$ ) of the absorbing material by the equation  $b^2 = 0.165T/A + \xi^2$ , where  $b$  and  $\xi$  have units of  $\text{km s}^{-1}$ ,  $T$  is in kelvins, and  $A$  is the atomic weight of the atomic species in question. The parameters of our best fit are listed in Table 2, where  $N_{\text{Mg II}}$  is the column density in units of  $\text{cm}^{-2}$ . The LISM velocity predicted for the 61 Cyg A line of sight by the LIC flow vector is  $-4.9 \text{ km s}^{-1}$ , which suggests that the component at  $-3.0 \pm 2.0 \text{ km s}^{-1}$  represents Mg II absorption from the local cloud. The high quality of the Mg II fit is indicated by its low  $\chi^2_v$  value ( $\chi^2_v = 0.504$ ), which is also listed in Table 2.

The Mg II absorption lines observed toward 40 Eri A were fitted in a similar fashion, except that only one com-

ponent was needed to adequately fit the data (see Fig. 4). The parameters of this fit are also given in Table 2. The measured velocity of  $21.8 \pm 1.0 \text{ km s}^{-1}$  is close to the velocity predicted by the LIC flow vector,  $23.3 \text{ km s}^{-1}$ .

#### 4. ANALYSIS OF THE Ly $\alpha$ LINES

##### 4.1. 61 Cyg A

In describing our analysis of the Ly $\alpha$  lines, we first focus on the 61 Cyg A data. In order to fit the H I and D I Ly $\alpha$  lines, it is first necessary to make an initial estimate for the shape of the stellar Ly $\alpha$  emission line, which is difficult because much of the line is absorbed by the highly saturated H I absorption feature. Following the example of previous analyses (Piskunov et al. 1997; Linsky & Wood 1996), we used the Mg II  $k$  line as a first estimate for the shape of the Ly $\alpha$  profile because both are very strong, highly optically thick chromospheric emission lines. For 61 Cyg A, we broadened the Mg II line by 70% in order to match the shape of the far wings of Ly $\alpha$ .

This Mg II model was only the starting point for our trial-and-error approach to modeling the stellar Ly $\alpha$  line. Many different variations on this initial theme were tried before final fit parameters and errors were ascertained. Some variations were made simply to maximize the quality of the fit and some variations were tried specifically to help estimate the systematic errors associated with this analysis. Basically, we see how much we can vary the stellar profile and still be able to accurately fit the data. Uncertainties are estimated based on how much the fit parameters vary within the subset of “good fits.” Nevertheless, we will only present representative “best fits” in this paper, as it is impractical to present all the fits attempted in this process.

The Mg II lines of both 61 Cyg A and 40 Eri A are well centered on the stellar radial velocity. This is not surprising, as we are not aware of any examples of main-sequence stars with strong chromospheric lines significantly shifted out of the stellar rest frame. The Sun’s quiescent chromospheric lines, including Mg II and Ly $\alpha$ , are centered on the photospheric rest frame, and GHRS data have shown this to be the case on many other solar-like stars (Wood, Linsky, & Ayres 1997; Wood 1996). Thus, for all considered stellar Ly $\alpha$  profiles, we require that the wings of Ly $\alpha$  be centered on the rest frame of the star, which turns out to be a very important constraint. To ensure that this is the case, we model the red wing by reflecting the blue wing onto the red side of the profile, with the stellar radial velocity (listed in § 2) used as the axis of symmetry.

Figure 5 shows our simplest fit to the 61 Cyg A Ly $\alpha$  line, assuming only the two LISM components detected in Mg II. The fit will be discussed in detail below; here we only want to emphasize that the amount of H I absorption seen in the red wing near  $1215.95 \text{ \AA}$  is determined almost solely by the requirement that the wings of the stellar emission line be centered on the stellar rest frame. This essentially determines the H I column density all by itself, in the absence of other complications such as stellar H-wall absorption (see below). The symmetrization of the stellar line profile is an effective constraint on the LISM column only because of the large velocity difference between the stellar emission and the LISM absorption, which results in far more H I absorption in the red wing than in the blue wing.

In all of our Ly $\alpha$  fits, we fit both the H I and D I lines simultaneously. We use Voigt functions to represent the

TABLE 2  
Mg II PARAMETERS

Star	Velocity ( $\text{km s}^{-1}$ )	$b_{\text{Mg II}}$ ( $\text{km s}^{-1}$ )	$\log N_{\text{Mg II}}$	$\chi^2_v$
61 Cyg A.....	$-3.0 \pm 2.0$	$3.0 \pm 0.4$	$12.4 \pm 0.2$	0.504
	$-9.0 \pm 1.0$	$3.0 \pm 0.4$	$13.0 \pm 0.2$	0.504
40 Eri A.....	$21.8 \pm 1.0$	$2.4 \pm 0.2$	$12.47 \pm 0.03$	1.409

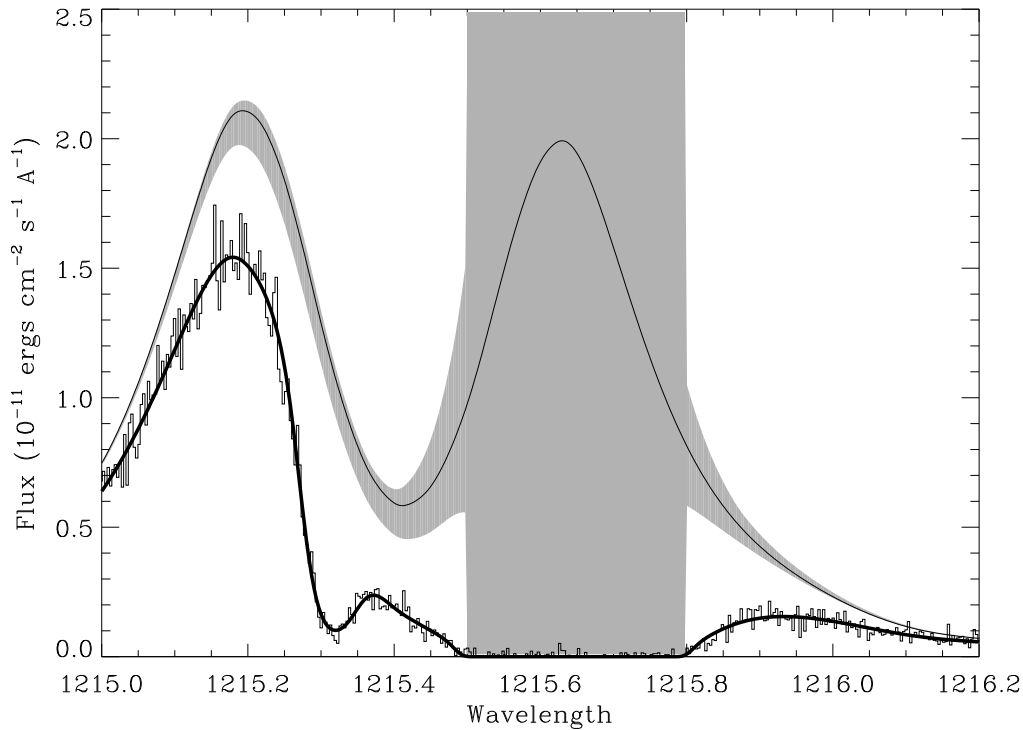


FIG. 5.—Fit to the H I and D I absorption lines seen toward 61 Cyg A (at 1215.65 and 1215.3 Å, respectively) using only the two interstellar absorption components detected in Fig. 3. The thin solid line is the assumed stellar Ly $\alpha$  profile, and the shaded region surrounding it shows the uncertainties in this profile, which are infinite within the saturated H I absorption line. The thick solid line is the fit to the data.

opacity profiles, and we account for both fine structure components of the H I and D I lines, which are separated by only 1.33 km s<sup>-1</sup>. The D I and H I line velocities are assumed to be identical. Since previous analyses have demonstrated that the H I and D I lines are dominated by thermal broadening, we force the H I and D I Doppler parameters to be consistent with the relation  $b_{\text{DI}} = b_{\text{HI}}/2^{1/2}$ . Our analysis is complicated by the existence of two LISM components toward 61 Cyg A, as seen in Mg II. We include the two LISM components in our Ly $\alpha$  fit, but these components are so highly blended for both H I and D I that additional constraints must be added. We assume the velocities measured in the Mg II fit ( $-3$  and  $-9$  km s<sup>-1</sup>) are applicable to H I and D I, and since we were forced to assume identical Doppler parameters for the two components of Mg II, we make the same assumption for Ly $\alpha$ . We also must assume that both components have the same D/H ratio to make the problem tractable. The four remaining free parameters are the H I column density of component 1, the H I column density of component 2, the H I Doppler parameter of both components, and the D/H ratio of both components.

We first try to fit the line with only LISM absorption, and Figure 5 shows the result. The parameters of the fit are listed in Table 3. By considering both the  $b_{\text{HI}}$  and  $b_{\text{Mg II}}$  values, the Doppler parameters can be separated into their thermal and nonthermal components. Thus, we also list in Table 3 the derived LISM temperature ( $T$ ) and nonthermal velocity ( $\xi$ ). These values ( $T = 7200 \pm 600$  K and  $\xi = 2.0 \pm 0.8$  km s<sup>-1</sup>) agree very well with the values previously measured for the LISM using GHRS data (Piskunov et al. 1997; Dring et al. 1997; Wood et al. 1996). The D/H ratio that we measure,  $D/H = (1.4 \pm 0.2) \times 10^{-5}$ , is also consistent with previous results (Piskunov et al. 1997; Dring et al. 1997).

Although the non-LIC absorption component is much stronger in Mg II than the LIC component, our Ly $\alpha$  fit suggests that the two components have nearly equal H I column densities ( $\log N_{\text{HI}} = 17.87 \pm 0.03$  and  $\log N_{\text{HI}} = 17.85 \pm 0.07$ ). We can estimate Mg abundances for both components by subtracting  $\log N_{\text{HI}}$  from  $\log N_{\text{Mg II}}$ . By subtracting the solar logarithmic Mg abundance ( $-4.41$ ; Anders & Grevesse 1989) from these values, we can derive logarithmic Mg depletion values,  $D(\text{Mg})$ , which are quoted

TABLE 3  
Ly $\alpha$  FITS WITHOUT A STELLAR H-WALL COMPONENT

Source of Absorption	Velocity (km s <sup>-1</sup> )	$b_{\text{HI}}$ (km s <sup>-1</sup> )	$T(10^3 \text{ K})$	$\xi$ (km s <sup>-1</sup> )	$\log N_{\text{HI}}$	D/H ( $\times 10^{-5}$ )	$D(\text{Mg})$
61 Cyg A:							
LISM (LIC).....	$(-3.0 \pm 2.0)$	$11.0 \pm 0.4$	$7.2 \pm 0.6$	$2.0 \pm 0.8$	$17.87 \pm 0.03$	$1.4 \pm 0.2$	$-1.06 \pm 0.30$
LISM.....	$(-9.0 \pm 1.0)$	$11.0 \pm 0.4$	$7.2 \pm 0.6$	$2.0 \pm 0.8$	$17.85 \pm 0.07$	$1.4 \pm 0.2$	$-0.44 \pm 0.30$
40 Eri A:							
LISM (LIC).....	$21.6 \pm 1.0$	$11.5 \pm 0.2$	$7.95 \pm 0.35$	$<1.2$	$17.94 \pm 0.03$	$1.11 \pm 0.09$	$-1.06 \pm 0.05$
Geocorona.....	$(-24.6)$	$5.2 \pm 0.6$	$1.6 \pm 0.4$	...	$12.96 \pm 0.05$	...	...

NOTE.—Values in parentheses are assumed rather than derived.

in the last column of Table 3. The significant depletions are presumably due to much of the interstellar Mg being locked up in dust grains. Note, however, that we have not taken into account the fact that roughly one-half of the hydrogen in the LISM is ionized (Wood & Linsky 1997), meaning that the actual depletion should be about 0.3 dex smaller than suggested by the  $D(\text{Mg})$  values in Table 3.

The LIC Mg depletion toward 61 Cyg A,  $D(\text{Mg}) = -1.06 \pm 0.30$ , is nearly identical to Mg depletions previously measured for the LIC toward Capella, Procyon, and HR 1099 (Linsky et al. 1995; Piskunov et al. 1997) and 40 Eri A as well (see below). This is an encouraging result that supports the accuracy of the H I column densities measured by our Ly $\alpha$  fit. Apparently, Mg is less depleted in the non-LIC cloud seen toward 61 Cyg A (see Table 3). Even lower Mg depletions have been reported toward  $\alpha$  Cen and  $\beta$  Cet (Linsky & Wood 1996; Piskunov et al. 1997).

Although the parameters of the Ly $\alpha$  fit in Figure 5 appear to be sensible, there is one major problem—the stellar profile assumed for this fit has a self-reversal that we believe to be unrealistically deep. In order to assess the necessity of this self-reversal, we estimated the uncertainties in the assumed stellar profile using the following technique. We slowly increase the fluxes of the assumed profile by adding randomly generated Gaussians to it, performing a fit to the data after each added Gaussian until we repeatedly find that we cannot change the profile further without the resulting fit either being a poor match to the data or having parameters inconsistent with the best-fit parameters and uncertainties given in Table 3. This gives us the upper bound to the shaded region in Figure 5. In order to derive the lower bound, we repeat this procedure but subtract the Gaussians rather than add them. Within the saturated H I absorption line core, the profile uncertainties are assumed to be infinite because there are no real constraints to the profile in this spectral region.

The H I column density uncertainties reported in Table 3 are fairly small, thanks mostly to our requirement that the stellar Ly $\alpha$  profile be centered on the stellar radial velocity, so the uncertainties in our assumed stellar profile also turn out to be reasonably small, except in the region of saturated absorption. Thus, without the inclusion of an additional absorption component, it is clear that the large self-reversal of the stellar Ly $\alpha$  line is indeed necessary to fit the data. The low fluxes observed near 1215.4 Å cannot be accounted for by the interstellar H I and D I absorption, so a deep self-reversal is the only remaining possibility. However, such a profile seems unlikely for several reasons. First of all, 40 Eri A (K1 V) is a star very similar to 61 Cyg A (K5 V), but the Ly $\alpha$  line of 40 Eri A does not appear to have a deep self-

reversal, as Figure 1 shows that the 40 Eri A Ly $\alpha$  spectrum does not have the dearth of flux near line center (0 km s<sup>-1</sup>) that the 61 Cyg A spectrum has.

For slowly rotating main-sequence stars, the depth of the Mg II self-reversals appears to be dependent on spectral type, with the earlier spectral types having the deeper reversals. (See the Mg II data presented by Wood 1996, Linsky & Wood 1996, and Linsky et al. 1995, in addition to that presented in this paper.) Thus, if Mg II is any guide, we would expect the Ly $\alpha$  line of 61 Cyg A (K5 V) to have a shallower self-reversal than the Ly $\alpha$  lines of 40 Eri A (K1 V) and the Sun (G2 V), but this is clearly not the case if the model in Figure 5 is correct. (For the solar Ly $\alpha$  profile, see Linsky & Wood 1996 or Brekke et al. 1991.) The Mg II lines of 61 Cyg A do not suggest that 61 Cyg A would deviate from this trend. We conclude that the Ly $\alpha$  profile in Figure 5 is unlikely, but we cannot decisively rule it out.

Without a deep self-reversal for the stellar Ly $\alpha$  line, the only way to fit the 61 Cyg A data is to add another absorption component. One possibility is to simply use an absorption component that exactly mimics the self-reversal of the stellar Ly $\alpha$  line in Figure 5. The problem with such a model lies in interpreting this absorption component. Its parameters would not be consistent with those expected for a stellar H wall. The velocity is especially wrong, as the absorption component is too blueshifted. The temperature would also be lower than expected, as will become apparent later (see § 5.1). The solar H wall can be immediately ruled out as a possible source of the additional absorption, as it would produce absorption on the red rather than on the blue side of the H I absorption line.

In Figure 6, we present a fit to the Ly $\alpha$  line with an additional absorption component (*dashed line*) that *can* be associated with a stellar H wall. A deep self-reversal is no longer needed for the assumed stellar emission line. The parameters of this fit are given in Table 4. Note that except for a small decrease in column density, the properties of the two LISM components have not changed at all from the fit in Figure 5 (see Table 3). The second absorption component has a velocity ( $-30 \pm 10$  km s<sup>-1</sup>) that lies between the stellar and LISM velocities ( $-64.5$  and  $-9$  km s<sup>-1</sup>, respectively), as one would expect for the decelerated interstellar material in a stellar H wall. The temperature of the component is extremely high ( $180,000 \pm 20,000$  K), implying a hotter H wall than any of those previously detected (see § 1). This is expected, however, because of the particularly large speed of 61 Cyg A through the LISM (85.0 km s<sup>-1</sup>), which makes for a more energetic collision. One might think that hydrogen would be completely ionized at these high temperatures, making the existence of a substantial

TABLE 4  
Ly $\alpha$  FITS WITH A STELLAR H-WALL COMPONENT

Source of Absorption	Velocity (km s <sup>-1</sup> )	$b_{\text{HI}}$ (km s <sup>-1</sup> )	$T(10^3 \text{ K})$	$\xi$ (km s <sup>-1</sup> )	$\log N_{\text{HI}}$	D/H ( $\times 10^{-5}$ )	$D(\text{Mg})$
61 Cyg A:							
LISM (LIC).....	$(-3.0 \pm 2.0)$	$11.0 \pm 0.4$	$7.2 \pm 0.6$	$2.0 \pm 0.8$	$17.83 \pm 0.07$	$(1.5 \pm 0.4)$	$-1.02 \pm 0.30$
LISM.....	$(-9.0 \pm 1.0)$	$11.0 \pm 0.4$	$7.2 \pm 0.6$	$2.0 \pm 0.8$	$17.83 \pm 0.09$	$(1.5 \pm 0.4)$	$-0.42 \pm 0.30$
Stellar H wall.....	$-30 \pm 10$	$55 \pm 3$	$180 \pm 20$	...	$14.10 \pm 0.20$	...	...
40 Eri A:							
LISM (LIC).....	$21.4 \pm 1.0$	$11.6 \pm 0.3$	$8.1 \pm 0.5$	$<1.2$	$17.85 \pm 0.10$	$(1.5 \pm 0.4)$	$-0.97 \pm 0.10$
Stellar H wall.....	$1 \pm 15$	$77 \pm 9$	$360 \pm 80$	...	$13.75 \pm 0.20$	...	...
Geocorona.....	$(-24.6)$	$5.2 \pm 0.6$	$1.6 \pm 0.4$	...	$12.96 \pm 0.05$	...	...

NOTE.—Values in parentheses are assumed rather than derived.

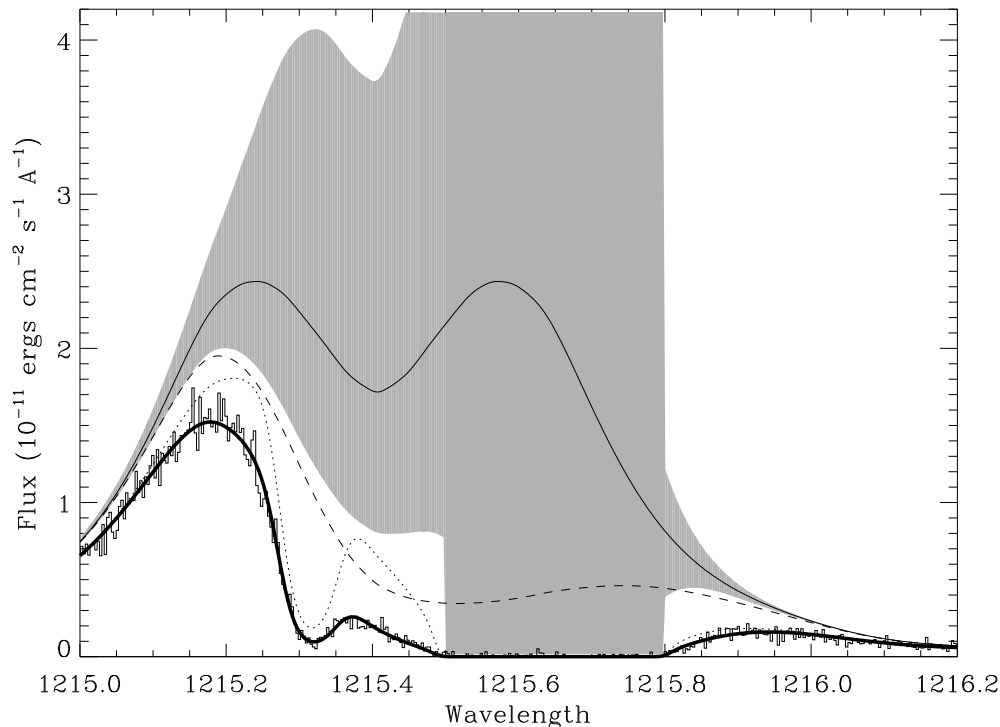


FIG. 6.—Fit to the Ly $\alpha$  line of 61 Cyg A, with a stellar H-wall absorption component included in addition to the two interstellar absorption components. The thin solid line is the assumed stellar Ly $\alpha$  profile, and the shaded region surrounding it shows the uncertainties in this profile, which are infinite within the saturated H I absorption line. The H-wall absorption is shown as a dashed line, the interstellar H I and D I absorption is represented by a dotted line, and the combination of these absorption components is shown as a thick solid line, which fits the data.

neutral H wall impossible. This is not the case, however, because densities are too low to maintain collisional ionization equilibrium within the H wall (Wood et al. 1996). The hot neutral H I in the hydrogen wall is produced by charge exchange processes, not by collisions.

The large H-wall temperature has resulted in a very broad absorption feature (see Fig. 6). This absorption component is in fact broad enough to contribute to the observed H I absorption in the red wing of the line near 1215.9 Å, which makes it very difficult to find a unique fit. The importance of the emission line symmetrization about the stellar radial velocity has been discussed above, but this procedure is no longer effective in accurately constraining the interstellar H I column density now that an additional absorption component has been added that also contributes to the absorption in the red wing and does so in a very different manner than the interstellar components.

Thus, we were forced to provide an additional constraint for the fit. We chose to constrain the LISM H I column density by forcing D/H to equal  $(1.5 \pm 0.4) \times 10^{-5}$ . This value is based on a compilation of GHRs D/H measurements (Linsky & Wood 1997), most of which are listed in Piskunov et al. (1997) and Dring et al. (1997), that yields a best D/H value for the LIC of  $D/H = (1.50 \pm 0.10) \times 10^{-5}$  and a best D/H value for all nearby interstellar material (including non-LIC clouds) of  $D/H = (1.47 \pm 0.18) \times 10^{-5}$ . We wanted to be conservative in the range of values we accept for D/H, so we have adopted an uncertainty in D/H ( $\pm 0.4 \times 10^{-5}$ ) that is substantially larger than the 1  $\sigma$  errors quoted above.

In Figure 6, we show the uncertainties in the stellar Ly $\alpha$  profile estimated using the Gaussian addition/subtraction technique described above. The profile uncertainties are

much larger than in Figure 5 because there are more free parameters in this fit, allowing good fits to be obtained using a much wider range of stellar profiles. The large shaded region in Figure 6 implies that very large changes must be made to the assumed stellar profile before the resulting fit parameters fall outside the error bars for the best-fit parameters in Table 4.

Finally, we investigated the possibility that the solar H wall might be affecting the H I absorption profile. The solar H wall probably extends out to the 61 Cyg A line of sight, which is at an angle of 79° from the upwind direction. Using the same solar H-wall temperature and column density measured by Linsky & Wood (1996) and assuming a velocity near the solar rest frame, we find that the solar H wall might make a small contribution to the H I absorption on the red side of the line, but we do not attempt to correct for it. Since our “best fit” already has three components, it would be unwise to increase the number of free parameters even further by adding a fourth.

#### 4.2. 40 Eri A

The 40 Eri A data were analyzed in much the same way as the 61 Cyg A data. Although we had to assume only one LISM component for the 40 Eri A line of sight, we did have to include a narrow absorption component to account for the presence of geocoronal absorption. In order to reduce the number of free parameters, we force the geocoronal Ly $\alpha$  absorption to be at its expected velocity of  $-24.6 \text{ km s}^{-1}$ . Figure 7 shows our best fit with the single LISM component (*dotted line*) and the geocoronal component (*dashed line*). The parameters of the fit are listed in Table 3.

The temperature and density of neutral hydrogen at a height of 400 km above the Earth are roughly 1100 K and



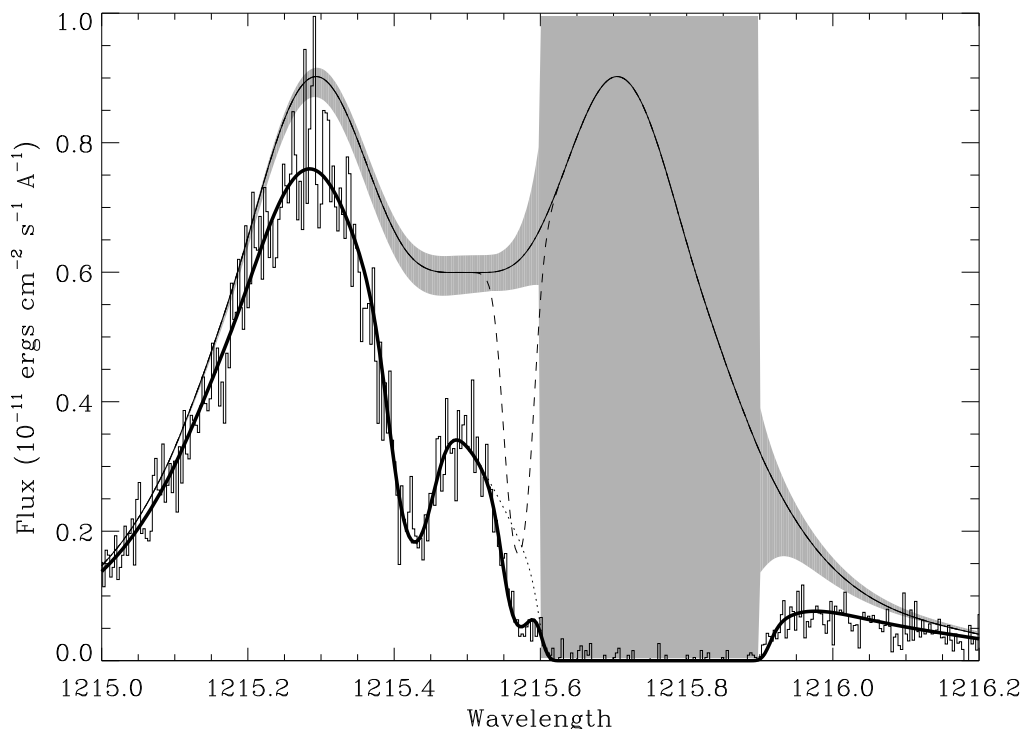


FIG. 7.—Fit to the H I and D I absorption lines seen toward 40 Eri A (at 1215.75 and 1215.4 Å, respectively) using only an interstellar absorption component and a geocoronal absorption component. The thin solid line is the assumed stellar Ly $\alpha$  profile, and the shaded region surrounding it shows the uncertainties in this profile, which are infinite within the saturated H I absorption line. The interstellar H I and D I absorption is shown as a dotted line, the narrow geocoronal absorption is represented by a dashed line, and the combination of these absorption components is shown as a thick solid line, which fits the data.

$1 \times 10^5 \text{ cm}^{-3}$ , respectively (Hedin 1983; Breig et al. 1976). The *Hubble Space Telescope* actually orbits a bit higher than this at about 600 km above the Earth, and the line of sight toward 40 Eri A samples even greater heights, so we might expect the average geocoronal H I density along the line of sight to be somewhat lower than  $1 \times 10^5 \text{ cm}^{-3}$  and the average temperature to be a bit higher than 1100 K. Nevertheless, if the geocorona extends roughly 1000 km along the 40 Eri A line of sight with an average density of  $10^5 \text{ cm}^{-3}$ , the expected H I column density is about  $10^{13} \text{ cm}^{-2}$ . This agrees very well with the column density we measure ( $\log N_{\text{HI}} = 12.96 \pm 0.05$ ). The geocoronal temperature listed in Table 3 ( $T = 1600 \pm 400 \text{ K}$ ) is also consistent with expectations. Note that we have had to assume that nonthermal velocities are negligible in order to compute a temperature from the measured Doppler parameter ( $b_{\text{HI}} = 5.2 \pm 0.6 \text{ km s}^{-1}$ ).

This is not the first time that geocoronal H I has been detected in Ly $\alpha$  absorption in GHRS data. In their analysis of the Ly $\alpha$  line of Capella, Linsky et al. (1993) reported the existence of two possible absorption features contaminating their data, but they did not recognize that one of them was located at exactly the velocity expected for geocoronal absorption ( $-22 \text{ km s}^{-1}$ ). We have reproduced the Linsky et al. (1993) fit of the interstellar absorption line in order to measure the geocoronal absorption seen toward Capella. The temperature and column density we measure for this line of sight are  $T = 2500 \pm 800 \text{ K}$  and  $\log N_{\text{HI}} = 12.58 \pm 0.07$ , respectively. These values differ somewhat from the 40 Eri A measurements, but some deviation is expected for completely different lines of sight measured at completely different times.

The temperature ( $7950 \pm 350 \text{ K}$ ), nonthermal velocity ( $\xi < 1.2 \text{ km s}^{-1}$ ), and Mg depletion [ $D(\text{Mg}) = -1.06 \pm 0.05$ ] of the LISM component in Figure 7 are all consistent with previous measurements of the LIC, and unlike the initial 61 Cyg A fit, we have no concern about the shape of the assumed stellar emission line. There is only one aspect of the fit that suggests a possible problem with this model of the absorption line—the D/H ratio. The D/H ratio of the fit,  $D/H = (1.11 \pm 0.09) \times 10^{-5}$ , is by far the lowest that has been measured from GHRS data for the LIC. As mentioned above, Linsky & Wood (1997) have derived a value of  $D/H = (1.50 \pm 0.10) \times 10^{-5}$  for the LIC based on a compilation of GHRS results, where the quoted error is the  $1 \sigma$  standard deviation of the measurements. Even if GHRS measurements of other nearby clouds are included, which are generally not as precise, the average value of D/H remains roughly the same ( $D/H = 1.47 \times 10^{-5}$ ), and the standard deviation increases only to  $\pm 0.18 \times 10^{-5}$ . Thus, our D/H ratio for the 40 Eri A line of sight appears to be truly discrepant from previous LIC measurements. The uncertainty in our D/H value is surprisingly small, thanks to the requirement that the stellar emission line wings be centered on the stellar rest frame, as discussed in § 4.1.

To date, the substantial reported variations of D/H in the LISM based on *IUE* and *Copernicus* data have not been supported by analyses of much higher quality GHRS data. Thus, the fit in Figure 7 would appear to be the strongest evidence yet for a variable D/H ratio within the LISM. This would be a very important result because measuring D/H and its variations is crucial for understanding Galactic chemical evolution and for cosmology in general (see

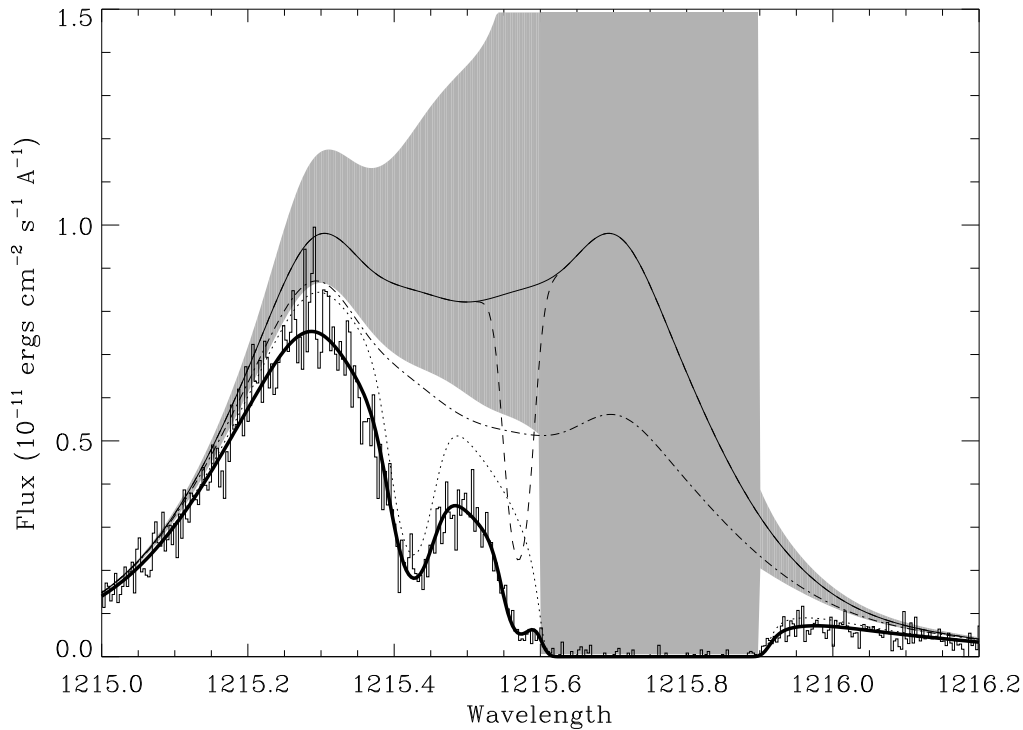


FIG. 8.—Fit to the Ly $\alpha$  line of 40 Eri A, with a stellar H-wall absorption component included in addition to the interstellar and geocoronal absorption components. The thin solid line is the assumed stellar Ly $\alpha$  profile, and the shaded region surrounding it shows the uncertainties in this profile, which are infinite within the saturated H I absorption line. The H-wall absorption is shown as a dot-dashed line, the interstellar H I and D I absorption is indicated by a dotted line, the geocoronal absorption is represented by a dashed line, and the combination of these absorption components is shown as a thick solid line, which fits the data.

Linsky et al. 1993, 1995). However, we will now show that the expected LIC D/H ratio can be recovered simply by adding a stellar H-wall absorption component with reasonable parameters.

Figure 8 shows our best fit to the 40 Eri A data when a stellar H-wall component (*dot-dashed line*) is included. The uncertainties in the stellar Ly $\alpha$  profile (*shaded region*) are found to be much larger than the profile uncertainties in the fit without an H-wall component (see Fig. 7), as was the case for 61 Cyg A. The parameters of the fit in Figure 8 are given in Table 4. The velocity of 40 Eri A through the LISM ( $123.2 \text{ km s}^{-1}$ ) is even faster than 61 Cyg A, so the extremely high temperature of the stellar H wall ( $360,000 \pm 80,000 \text{ K}$ ) and the correspondingly broad absorption are as expected. This broad component contributes to the absorption in the red wing of the line, reducing the amount of interstellar H I absorption and thereby increasing D/H. The other LISM

parameters do not change much. In practice, we ended up forcing  $D/H = (1.5 \pm 0.4) \times 10^{-5}$  to adequately constrain the fit, as we did in § 4.1 for 61 Cyg A. Note that we do not expect to see any solar H-wall absorption at all for the 40 Eri A line of sight because it is in a downwind direction from the Sun,  $155^\circ$  from the upwind direction to be precise.

## 5. WHAT CAN WE LEARN FROM HYDROGEN WALLS?

### 5.1. Comparison of Measured Hydrogen-Wall Properties with Theoretical Expectations

In Table 5, we summarize the properties of the six stellar H walls that have been at least tentatively detected to date. Listed in the table are the stars, their spectral types, their distances from the Sun ( $d$ ), their velocities through the LISM ( $v$ ), and the angle between the upwind direction and the line of sight sampled by the GHRS observations ( $\theta$ ). We

TABLE 5  
COMPILATION OF DETECTED STELLAR H WALLS

Star (1)	Spectral Type (2)	$d$ (pc) (3)	$v$ ( $\text{km s}^{-1}$ ) (4)	$\theta$ (deg) (5)	$v_{\text{HW}} - v_{\text{ISM}}$ ( $\text{km s}^{-1}$ ) (6)	$T_{\text{HW}}$ ( $\times 10^3 \text{ K}$ ) (7)	$\log N_{\text{HW}}$ (8)	$R$ ( $R_\odot$ ) (9)	$P_{\text{wind}}(R)/P_\odot$ (10)	$\log F_x$ (11)
Sun .....	G2 V	...	25.6	52	$> 2$	$29 \pm 5$	$14.74 \pm 0.24$	1.0	1.00	4.21
$\epsilon$ Eri .....	K1 V	3.3	25.9	77	$-12 \pm 6$	$28 \pm 5$	$14.3 \pm 0.2$	0.8	0.22	5.86
$\lambda$ And .....	G8 IV–III+?	23	47.7	89	$-8 \pm 3$	$62 \pm 18$	$14.8 \pm 0.2$	7.0	0.09	6.09
$\epsilon$ Ind .....	K5 V	3.5	64.0	60	$-18 \pm 6$	$100 \pm 20$	$14.2 \pm 0.2$	0.7	1.06	4.71
61 Cyg A .....	K5 V	3.5	85.0	46	$-21 \pm 10$	$180 \pm 20$	$14.1 \pm 0.2$	0.7	1.18	4.79
40 Eri A .....	K1 V	4.8	123.2	58	$-20 \pm 15$	$360 \pm 80$	$13.75 \pm 0.20$	0.8	0.38	5.01

also list the three parameters measured for the hydrogen walls: the H-wall temperature ( $T_{\text{HW}}$ ), the H I column density ( $N_{\text{HW}}$ ), and the H-wall flow velocity ( $v_{\text{HW}}$ ), which in Table 5 is listed relative to the line-of-sight ISM velocity ( $v_{\text{ISM}}$ ).

For all of the stellar H walls, the  $v_{\text{HW}} - v_{\text{ISM}}$  velocities are negative. This is mostly due to the deceleration of the interstellar material as it crosses the bow shock and enters the H wall, but for more sidestream lines of sight ( $\theta \approx 90^\circ$ ) it is partly due to the deflection of H-wall material away from the heliosphere (Baranov & Malama 1993). Note that for the solar H wall, these effects result in a positive rather than a negative value for  $v_{\text{HW}} - v_{\text{ISM}}$  because we are observing the flow changes from within the heliosphere. We do not attempt to compare the measured  $v_{\text{HW}} - v_{\text{ISM}}$  values with any theoretical predictions because this quantity should be a sensitive function of both  $v$  and  $\theta$ .

Of the three measured H-wall properties, the temperature is potentially the most interesting because Table 5 indicates a strong correlation between  $v$  and  $T_{\text{HW}}$  that can be compared with the predictions of shock jump conditions. As a rough approximation to actual stellar bow shocks, we consider the case of an interstellar wind with velocity,  $v_1$ , that is normally incident onto an ideal hydromagnetic shock. The interstellar magnetic field,  $B_1$ , is assumed to be parallel to the shock. (Note that in the case of normally incident flow, any component of  $B$  perpendicular to the shock will be irrelevant for the jump conditions of interest.)

Following the example of Shu (1992; see Chap. 25), we reduce the ideal MHD equations to the following quadratic expression:

$$\gamma(\gamma + 1)\eta^2 - \left[ \gamma(\gamma - 1) + (\alpha + 1) \frac{2\gamma}{M^2} \right] \eta - (2 - \gamma) \frac{2\alpha}{M^2} = 0, \quad (1)$$

where  $\eta \equiv \rho_1/\rho_2$  (the preshock to postshock density ratio),  $M$  is the preshock acoustic Mach number ( $M \equiv v_1/c_1$ ), and  $\alpha$  is the ratio of magnetic pressure to thermal pressure for the interstellar gas ( $\alpha \equiv B_1^2/8\pi P_1$ ). Assuming solar abundances, the sound speed in the LISM is

$$c_1 = \left( \frac{\gamma n_1 k T_1}{\rho_1} \right)^{1/2} = \left[ 0.7(x + 1) \frac{\gamma k T_1}{m_p} \right]^{1/2}, \quad (2)$$

where  $m_p$  is the proton mass, and  $x$  is the ionization fraction for hydrogen in the LISM. Thus, if  $\gamma = 5/3$  and  $v_1$  is in units of  $\text{km s}^{-1}$ ,

$$M = 10.2 \frac{v_1}{\sqrt{(x + 1)T_1}}. \quad (3)$$

Solving for  $\eta$  in equation (1) and assuming once again that  $\gamma = 5/3$ , we find

$$\eta = \frac{1}{8} \left[ 1 + 3 \frac{\alpha + 1}{M^2} + \sqrt{9 \left( \frac{\alpha + 1}{M^2} \right)^2 + \frac{4}{M^2} \left( \frac{39}{10} \alpha + \frac{3}{2} \right) + 1} \right]. \quad (4)$$

The energy flux,

$$q_0 \equiv \frac{\gamma}{\gamma - 1} P v + \frac{1}{2} \rho v^3 + \frac{v B^2}{4\pi}, \quad (5)$$

is the same on both sides of the shock front. Using the jump conditions  $\eta \equiv \rho_1/\rho_2 = B_1/B_2 = v_2/v_1$  (Shu 1992), one can use equation (5) to derive the following expression for the pressure ratio across the shock:

$$\frac{P_2}{P_1} = \frac{30\eta + (1 - \eta)[10M^2\eta(\eta + 1) - 24\alpha]}{30\eta^2}. \quad (6)$$

Since  $T_2/T_1 = \eta P_2/P_1$ , the temperature ratio is then

$$\frac{T_2}{T_1} = 1 + \frac{(1 - \eta)[5M^2\eta(\eta + 1) - 12\alpha]}{15\eta}. \quad (7)$$

Using equations (3), (4), and (7), we plot, in Figure 9, the expected temperature ratio as a function of  $v_1$  for three values of  $x$  and two values of  $\alpha$ . We also display the measured temperature ratios for the six stars with detected H walls, based on the temperatures listed in Table 5 ( $T_2 = T_{\text{HW}}$ ,  $v_1 = v$ ). The average LISM temperature measured for all the lines of sight listed in Piskunov et al. (1997) and Dring et al. (1997) is 8000 K, so this is the value we assume for  $T_1$ . In general, the agreement between the data and the theoretical curves in Figure 9 is quite good, especially for the  $\alpha = 0$ ,  $x = 0.5$  case. For large  $v_1$ , the jump conditions predict  $T_2/T_1 \propto v_1^2$ , which agrees very well with the observed increase in H-wall temperature with  $v_1$ .

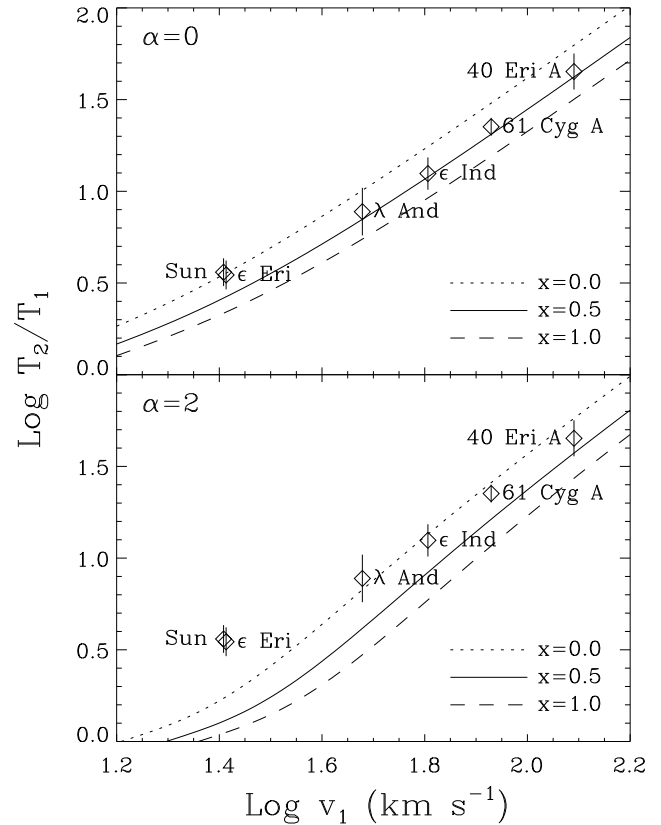


FIG. 9.—For all the stars with detected H walls, we plot the ratio of the measured hydrogen-wall temperature ( $T_2$ ) to the interstellar temperature ( $T_1 = 8000$  K) versus the stellar velocity through the LISM ( $v_1$ ). The lines in the figure are theoretical predictions based on the hydromagnetic shock jump conditions. In the top (bottom) panel, the ratio of magnetic pressure to thermal pressure in the LISM is assumed to be  $\alpha = 0$  ( $\alpha = 2$ ). In each panel, theoretical curves are plotted for three assumed values of the hydrogen ionization fraction in the LISM ( $x = 0.0, 0.5$ , and  $1.0$ ).

The Sun and  $\epsilon$  Eri data points appear to be somewhat higher than expected based on the theoretical curves and the other data points. The work of Gayley et al. (1997) suggests that the H-wall temperature measured for the Sun by Linsky & Wood (1996) and used in Figure 9 may be too high. Using the same  $\alpha$  Cen observations as Linsky and Wood, Gayley et al. (1997) showed that the observed H I absorption could be reproduced by H-wall models with  $T \approx 16,000$  K (compared with  $T = 29,000 \pm 5000$  K from Linsky & Wood 1996), especially if stellar H-wall absorption from  $\alpha$  Cen is included to account for some of the H I absorption on the blue side of the profile. Thanks partly to this  $\alpha$  Cen absorption and partly to a solar H-wall deceleration larger than that measured by Linsky & Wood (1996), Gayley et al. (1997) are able to fit the data with a narrower, cooler, H-wall component.

Contamination of the  $\epsilon$  Eri data by the solar H wall should not be a problem, since the  $\epsilon$  Eri line of sight is far from the H wall at a mere  $36^\circ$  from the downwind direction. However, there is another reason  $T_{\text{HW}}$  might have been overestimated for  $\epsilon$  Eri as well as for the Sun. When  $T_{\text{HW}}$  is computed from the measured Doppler parameter, it is assumed that nonthermal velocities are insignificant (i.e.,  $\xi = 0 \text{ km s}^{-1}$ ), but this need not be the case. For one thing, the deceleration of interstellar material at the H-wall boundary does not happen instantaneously (see, e.g., Zank et al. 1996). Thus, there should be a distribution of flow velocities in the H wall. For the Sun, the heliospheric models of Gayley et al. (1997) predict decelerations of about  $10 \text{ km s}^{-1}$  toward  $\alpha$  Cen. If we therefore assume  $\xi = 10 \text{ km s}^{-1}$  as a very rough estimate for both the solar and  $\epsilon$  Eri H walls, the temperatures listed for these stars in Table 5 are decreased by about 6000 K to  $23,000 \pm 5000$  K and  $22,000 \pm 5000$  K, respectively; these values are much more consistent with both the predictions of the heliospheric models and the theoretical curves in Figure 9.

Another factor that must be mentioned is that heliospheric models suggest that the H-wall temperatures should be somewhat higher than the jump conditions predict. As described by Zank et al. (1996), some of the neutrals in the LISM that penetrate the heliopause charge exchange with very hot solar wind protons. Some of the resulting hot neutrals are carried back across the heliopause where some deposit their energy through further charge exchanges. This provides a heating source for the H wall in addition to the shock heating estimated by the jump conditions.

Is it possible that  $T_{\text{HW}}$  has been overestimated for  $\lambda$  And,  $\epsilon$  Ind, 61 Cyg A, and 40 Eri A, just as we argued it might have been for the Sun and  $\epsilon$  Eri? It is hard to say without computing the relevant astrospheric models. The thermal line broadening should be greater for the former stars owing to hotter H walls, but the effective nonthermal broadening could also be larger owing to more deceleration. Therefore, neglecting nonthermal broadening could be a significant source of uncertainty. However, we see no reason that the charge exchange (nonshock) heating process discussed in the previous paragraph should increase with  $v_1$  to the extent that the shock heating does, so we doubt that  $T_{\text{HW}}$  has been significantly overestimated owing to this effect, at least for the four hottest H walls.

There are several potential sources of systematic error in addition to those that have already been mentioned. For example, the interstellar flow is not actually perpendicular to the bow shock, since in no case are we looking exactly in

the upwind (i.e.,  $\theta = 0^\circ$ ) direction. Thus, the jump condition in equation (7) is only an approximation that will, if anything, overestimate the temperature increase. Another potential difficulty is that we have not included the effects of cosmic rays. The cosmic-ray pressure in the LISM is not known accurately, but it is thought to be comparable to the LISM thermal and magnetic pressures (Bloemen 1987; Ip & Axford 1985). The degree to which these cosmic rays couple to the thermal plasma and influence astrospheric structures is uncertain, but including a cosmic-ray pressure term would result in lower theoretical curves in Figure 9, generally degrading the agreement with the observations.

To summarize, the four major potential sources of systematic error that we have discussed are:

1. The neglect of nonthermal velocities in computing  $T_{\text{HW}}$ .
2. The presence of nonshock heating in the hydrogen walls.
3. The imprecise applicability of the plane-parallel, normal-incidence jump conditions to actual stellar bow shocks.
4. The neglect of cosmic-ray pressure.

While the first two errors serve to increase the measured temperatures, the last two serve to increase the theoretical temperatures, so these systematic errors should cancel to some extent.

Figure 9 suggests that the H-wall temperatures might be used to derive at least crude estimates for  $x$  and  $\alpha$ , estimates that may still be useful since  $x$  and  $\alpha$  are not well determined for the LISM. Considering all the uncertainties discussed above, especially that Gayley et al. (1997) were able to fit the  $\alpha$  Cen data with a solar H-wall temperature of only 16,000 K, we derive the following rough upper limits for  $x$  and  $\alpha$ :  $x < 0.6$  and  $\alpha < 2$ . The upper limit for  $x$  is consistent with the findings of Wood & Linsky (1997), who measured an ionization fraction of  $x = 0.45 \pm 0.25$  using observations of the C II  $\lambda\lambda 1335, 1336$  lines, which are sensitive to the electron density in the LISM.

For an assumed interstellar particle density of  $0.2 \text{ cm}^{-3}$ , the  $\alpha < 2$  upper limit suggests an upper limit for the LISM magnetic field of  $B < 5 \mu\text{G}$ . Observed pulsar rotation measures indicate that the global Galactic magnetic field has a magnitude of about  $1.6 \pm 0.2 \mu\text{G}$  in the LISM and is directed toward a Galactic longitude of  $l = 96^\circ \pm 4^\circ$  (Rand & Kulkarni 1989). However, both the pulsar data and observations of the background Galactic synchrotron emission suggest that the local magnetic field is dominated by random field components, estimates of which are generally in the range of  $3\text{--}9 \mu\text{G}$  (Rand & Kulkarni 1989; Heiles 1987; Beuermann, Kanbach, & Berkhuijsen 1985; Phillips et al. 1981a, 1981b). Our result suggests that values in the lower part of this range are more likely.

The plasma Mach number for the interstellar wind flowing into the heliosphere is

$$M_A = 2.93[(x + 1)(\alpha + 1)]^{-1/2}. \quad (8)$$

Thus, our upper limits for  $\alpha$  and  $x$  suggest that  $M_A$  is greater than 1.3. This implies that the interstellar wind near the Sun is supersonic and that a bow shock must therefore exist outside the heliosphere in the upwind direction. In contrast, Gayley et al. (1997) found that of their three heliospheric models, it was the slightly subsonic one ( $M_A = 0.9$ ) that

produced an H wall most consistent with the GHRs observations of  $\alpha$  Cen. This apparent discrepancy is probably illusory, however, as three models are not enough to adequately cover the allowable range of input parameters, and two of the three models actually assume an unreasonably high temperature for the LISM ( $T = 10,900$  K).

### 5.2. The Extent of the LIC

One of the requirements for a star to be encompassed by a hydrogen wall is that the star reside in a partially neutral, warm interstellar cloud such as the LIC. If the interstellar material surrounding a star is completely ionized, there will be no neutral particles available to form an observable H wall. Thus, a star will not have an H wall if it is in the so-called hot phase of the ISM, which has low density ( $n \sim 10^{-3} \text{ cm}^{-3}$ ), high temperature ( $T \sim 10^6$  K), and is fully ionized. The Sun resides within a region of space called the Local Bubble, in which most of the bubble's volume is thought to be filled with the hot ISM (Cox & Reynolds 1987). This could explain the observed soft X-ray background radiation and could explain why some long lines of sight, especially ones generally directed away from the Galactic center, have extremely low H I column densities. Examples include  $\epsilon$  CMa ( $d = 200$  pc,  $\log N_{\text{HI}} \approx 18.0$ ; Gry et al. 1995), 31 Com ( $d = 80$  pc,  $\log N_{\text{HI}} = 17.95$ ; Piskunov et al. 1997), and HR 1099 ( $d = 36$  pc,  $\log N_{\text{HI}} = 18.1$ ; Piskunov et al. 1997).

The highest average H I densities that have been measured toward nearby stars are all roughly  $n_{\text{HI}} = 0.1 \text{ cm}^{-3}$ , which is therefore assumed to be the average H I density of the LIC. For three of the stars with detected H walls ( $\epsilon$  Ind,  $\epsilon$  Eri, and 61 Cyg A), the observed interstellar column density is consistent with  $n_{\text{HI}} = 0.10 \pm 0.02 \text{ cm}^{-3}$ . Thus, it is not surprising that these stars lie within a warm H I cloud and therefore have H walls, although the second component seen toward 61 Cyg A suggests that this star lies not in the LIC but in an adjacent H I cloud with similar properties.

A significantly lower average density is seen toward  $\lambda$  And ( $n_{\text{HI}} = 0.040 \pm 0.014 \text{ cm}^{-3}$ ; Wood et al. 1996). The inference is that at least some of this line of sight might be occupied by hot ISM and that  $\lambda$  And might therefore be in a separate H I cloud. Unfortunately, there are no Mg II observations available to check for multiple absorption components, so we cannot say much more about this line of sight. However, the 40 Eri A line of sight also has a low average density ( $n_{\text{HI}} = 0.048 \pm 0.012 \text{ cm}^{-3}$ ; see Table 4), and the Mg II data are consistent with all of the interstellar absorption being from the LIC. Thus, if 40 Eri A really does have a stellar H wall and therefore cannot be in the hot ISM, then the LIC must extend in that direction at least to the 4.8 pc distance of 40 Eri A, and the LIC H I density must decrease from the Sun to 40 Eri A to account for the low average density. Either the total density must decrease or the hydrogen ionization fraction must increase. The implied existence of density and/or ionization fraction gradients in the LIC is not particularly surprising, but this is the first observational evidence we are aware of that suggests that such gradients actually exist.

### 5.3. The Stellar Winds of Solar-like Stars

Another requirement for a star to have an observable hydrogen wall is that the star must have a hot, ionized wind with a ram pressure roughly comparable to that of the solar

wind. Without such a wind, the H I pileup region will either not exist at all or will not be thick enough to have detectable H I absorption. Thus, we can infer that the stars with detected H walls all have stellar winds, and we can ponder whether or not the measured properties of the H walls can be used to deduce the attributes of these winds. We shall now describe how the H-wall column density might be used for this purpose.

The ram pressure of a stellar wind at some reference distance from the star,  $r_0$ , is  $P_{\text{wind}}(r_0) = \rho_{\text{wind}} v_{\text{wind}}^2$ . In the upwind direction, the wind pressure is balanced by the interstellar wind pressure at the termination shock. This interstellar wind pressure can be expressed as  $P_{\text{ISM}} = \rho_{\text{ISM}} v^2$ , where  $\rho_{\text{ISM}}$  is the interstellar density, and  $v$  is the velocity of the star through the LISM. Since  $P_{\text{wind}}(r)$  falls off as  $1/r^2$ , the distance to the termination shock is approximately

$$R_{\text{TS}}^2 = 0.88 \frac{P_{\text{wind}}(r_0)}{P_{\text{ISM}}} r_0^2, \quad (9)$$

where the 0.88 factor is meant to account for the reduction in pressure that occurs just outside the termination shock due to flows in that region (Parker 1963; Lee 1996). We are interested in comparing wind pressures of stars with different radii (especially  $\lambda$  And). In order to make for a more equitable comparison, we choose to evaluate  $P_{\text{wind}}$  at the surfaces of the stars, so we will set the reference radius,  $r_0$ , to be equal to the stellar radius,  $R$ .

The termination shock distance is indicative of the size scale of the entire astrosphere. Thus, the thickness of the hydrogen wall,  $h_{\text{HW}}$ , should be roughly proportional to  $R_{\text{TS}}$ . The H-wall column density can be expressed as  $N_{\text{HW}} = \rho_{\text{HW}} h_{\text{HW}}$ . In the strong shock limit,  $\rho_{\text{HW}} = 4\rho_{\text{ISM}}$  (see eq. [4]), and even for the solar case, which represents the weakest shock in our sample of stars, heliospheric models suggest that  $\rho_{\text{HW}}/\rho_{\text{ISM}} \approx 2-3$  (Zank et al. 1996; Pauls et al. 1995). Thus,  $\rho_{\text{HW}}$  should be roughly the same for all of our stars, as long as  $\rho_{\text{ISM}}$  is also roughly equivalent. Therefore, since  $N_{\text{HW}} \propto h_{\text{HW}} \propto R_{\text{TS}}$ , we can turn equation (9) into the following expression for the stellar wind pressure (at the stellar surface) relative to the solar wind pressure [ $P_{\odot} \equiv P_{\text{wind}}(R_{\odot})$ ],

$$\frac{P_{\text{wind}}(R)}{P_{\odot}} = \left( \frac{N_{\text{HW}}}{N_{\odot}} \frac{v}{v_{\odot}} \frac{R_{\odot}}{R} \right)^2. \quad (10)$$

Values for  $v$ ,  $v_{\odot}$ ,  $N_{\text{HW}}$ ,  $N_{\odot}$ , and  $R$  are listed in columns 4, 8, and 9 of Table 5. The  $\lambda$  And radius is from Dempsey et al. (1993). For the K stars, we simply assume typical radii for stars of that spectral type:  $R = 0.8 R_{\odot}$  for the K1 stars, and  $R = 0.7 R_{\odot}$  for the K5 stars. Values of  $P_{\text{wind}}(R)/P_{\odot}$  are computed using equation (10) for all the stars with detected H walls, and the results are shown in column 10 of Table 5.

The acceleration mechanism of these winds presumably lies in the stellar coronae, so one might expect  $P_{\text{wind}}$  to be dependent on the coronal properties of the stars. Therefore, in the last column of Table 5 we list coronal X-ray surface fluxes for these stars (in units of  $\text{ergs cm}^{-2} \text{ s}^{-1}$ ), using the stellar radii listed in Table 5 and X-ray luminosities measured by the Position Sensitive Proportional Counter (PSPC) onboard ROSAT. The average solar PSPC flux is from Ayres (1997), the  $\lambda$  And value is from Dempsey et al. (1993), and the X-ray fluxes of the four K stars are from Schmitt, Fleming, & Giampapa (1995).

It is difficult to predict how  $P_{\text{wind}}$  might vary with  $F_X$  based on our current limited understanding of solar/stellar winds. On one hand, magnetic fields play a vital role in many wind acceleration mechanisms such as MHD waves and coronal mass ejections, which suggests that  $P_{\text{wind}}$  should increase with  $F_X$ . On the other hand, a more magnetically active star will have more closed field lines that inhibit stellar wind flow, which suggests that  $P_{\text{wind}}$  should decrease with increasing  $F_X$ . The solar example demonstrates the importance of this latter effect. During its 11 year activity cycle, the solar X-ray luminosity in the *ROSAT* PSPC bandpass varies by about a factor of 4 (Ayres 1997; Hinteregger 1981). However, while  $F_X$  decreases by a factor of 4 from solar maximum to minimum, data from *Voyager 2* shows that the solar wind ram pressure actually *increases* by a factor of 2 (Lazarus & McNutt 1990). The larger pressure at minimum is due mostly to a higher average wind speed, but the particle density is larger as well.

In Figure 10, we plot  $\log P_{\text{wind}}(R)/P_{\odot}$  versus  $\log F_X$ . Two points are used to represent the Sun, one for solar minimum and one for solar maximum. A thick line connects these two points, and a dashed line extends this relation to larger values of  $F_X$ . This  $P_{\text{wind}} \propto F_X^{-1/2}$  relation is indeed consistent with our crude estimates of  $P_{\text{wind}}(R)/P_{\odot}$  for the other stars, as well as being consistent with the solar activity cycle variations. However, the error bars on these estimates are very large, and H walls must be detected around more stars, especially more active ones, before the  $P_{\text{wind}} \propto F_X^{-1/2}$  proportionality can truly be tested.

We were surprised to find that the  $\lambda$  And data point is consistent with the general trend of the other points plotted in Figure 10 because unlike the other stars,  $\lambda$  And is very different from the Sun. By evaluating  $P_{\text{wind}}$  at the stellar surface rather than at some arbitrary reference radius, we hoped to compensate for the star's large radius, but there are other reasons the  $\lambda$  And wind might be expected to behave differently from the others, including a substantially

lower surface gravity and the tidal effects of being in a close binary system. Nevertheless, Figure 10 suggests that the wind of  $\lambda$  And may not be fundamentally different from the others. As a word of caution, however, we note that the detection of the  $\lambda$  And H wall is the most questionable of all the H-wall detections (see Wood et al. 1996).

Figure 10 raises the possibility of extrapolating the relationships between  $F_X$  and solar wind properties seen during the solar activity cycle to other stars with larger  $F_X$  values. It then becomes possible to study stellar winds simply by measuring stellar X-ray fluxes. One can then, for example, estimate how mass loss varies with time for solar-like stars. Much progress has been made in the past two decades toward understanding how stellar activity (including X-ray emission) varies with rotation rate ( $v_{\text{rot}}$ ) and age ( $t$ ). As stars age, their rotation rates decrease, reducing the amount of magnetic field generated by the dynamos in their interiors. In particular, for stars like the Sun, Ayres (1997) finds

$$F_X \propto v_{\text{rot}}^{2.9 \pm 0.3} \quad (11)$$

and

$$v_{\text{rot}} \propto t^{-0.6 \pm 0.1} \quad (12)$$

The tentative  $P_{\text{wind}} \propto F_X^{-1/2}$  relation then predicts that the wind ram pressures of solar-like stars will evolve with time as

$$P_{\text{wind}} \propto t^{0.87 \pm 0.28} \quad (13)$$

To estimate the uncertainty given in the above relation, we assumed a 25% error for the exponent of  $F_X$  in the  $P_{\text{wind}} \propto F_X^{-1/2}$  relation. The mass-loss rate,  $\dot{M}$ , is often of more interest than  $P_{\text{wind}}$ . Since the solar mass-loss rate varies by about a factor of 1.5 during the activity cycle (Lazarus & McNutt 1990),  $\dot{M} \propto F_X^{-3/8}$ . Assuming once again a 25% error in the exponent of  $F_X$ , we then have

$$\dot{M} \propto t^{0.65 \pm 0.21} \quad (14)$$

Relations (13) and (14) imply that wind pressure and mass loss increase with time and that the solar wind should have been weaker in the past.

The issue of solar/stellar wind evolution is important for many reasons. The past history of the solar wind is very relevant to studies of the early history of planetary atmospheres in the inner solar system (Ayres 1997; Kass & Yung 1995; Luhmann & Bauer 1992). Since mass loss plays a vital role in the magnetic braking mechanism by which stars shed their angular momentum, the time dependence of this mass loss is also very relevant for studies of the angular momentum evolution of late-type stars (see, e.g., Krishnamurthi et al. 1997 and references therein). Note, however, that relations (13) and (14) will not apply for very young stars ( $t \lesssim 0.3$  Gyr), because relation (12) breaks down for such stars. Very young stars of similar age and spectral type are observed to have a broad range of rotational velocities, so no simple relation will be applicable at that age.

Equation (10), which is the source of all our estimates of  $P_{\text{wind}}$ , was derived on the basis of several approximations. In the future, it may be possible to test the validity of the equation. The GHRS observations of  $\alpha$  Cen used to detect the solar H wall were made near solar minimum. It would

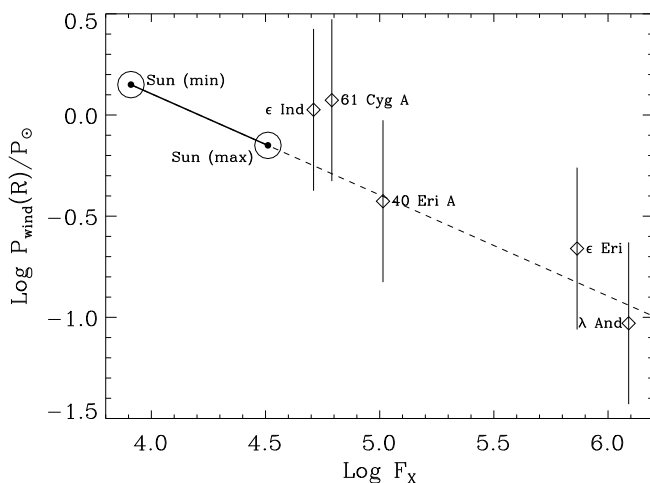


FIG. 10.—For all the stars with detected H walls, stellar wind pressures at the surfaces of the stars,  $P_{\text{wind}}(R)$ , have been estimated. These values are divided by the average solar wind pressure at the solar surface ( $P_{\odot}$ ) and then plotted versus measured X-ray surface fluxes. Two points are plotted for the Sun, one representing the Sun at solar maximum and the other representing the Sun at solar minimum. A thick solid line connects these two points, and a dashed line shows the extension of this line to higher values of  $\log F_X$ .

be useful to repeat these observations, using the Space Telescope Imaging Spectrograph (STIS) currently onboard *HST*, during the next solar maximum when  $P_{\text{wind}}$  should be lower by about a factor of 2 according to the *Voyager 2* observations of the previous solar cycle (Lazarus & McNutt 1990). Equation (10) predicts that  $N_{\text{HW}}$  should therefore be lower by a factor of  $2^{1/2}$ . This is enough of a change to produce a significantly different  $\text{Ly}\alpha$  absorption profile than that observed at solar minimum. The large uncertainties in the  $N_{\text{HW}}$  measurements in Table 5 indicate that it may be difficult to detect only a 30% decrease in  $N_{\text{HW}}$ , but we believe that direct comparison of the solar maximum and solar minimum data should make it clear whether  $N_{\text{HW}}$  has decreased by roughly the amount expected.

Finally, we note that the Sun is not the only star in our sample to have an activity cycle. The chromospheric Ca II H and K emissions of 61 Cyg A and 40 Eri A, which have been monitored for three decades, demonstrate that both stars have well-defined, solar-like activity cycles with periods of 7.3 and 10.1 yr, respectively (Baliunas et al. 1995). (The monitoring program also includes  $\epsilon$  Eri, but  $\epsilon$  Eri is typical of many active stars in that it does not appear to have a periodic activity cycle.) The GHRS observations of 61 Cyg A and 40 Eri A were obtained near the maxima of their activity cycles, so in the future it would be interesting to repeat these observations during the expected minima to see if the H-wall absorption changes in a manner consistent with equation (10). Detection of the expected changes would serve to verify the H-wall detections for 61 Cyg A and 40 Eri A, which otherwise are still subject to doubt (see § 4).

## 6. SUMMARY

We began this paper by analyzing the  $\text{Ly}\alpha$  and Mg II absorption lines seen toward 61 Cyg A and 40 Eri A. Our goals were to measure the interstellar parameters along these lines of sight and to search for evidence of stellar hydrogen walls, which are produced by collisions between the winds of the stars and the inflowing LISM. The quantitative results are given in Tables 3 and 4. We summarize these results as follows:

1. Analysis of the Mg II lines reveals the existence of two interstellar components toward 61 Cyg A, but only one component is seen toward 40 Eri A. The LISM flow velocities predicted for these lines of sight by the LIC (local interstellar cloud) vector of Lallement et al. (1995) agree reasonably well with the velocity of the single 40 Eri A LISM component and one of the two 61 Cyg A components.

2. We were able to fit the  $\text{Ly}\alpha$  line of 61 Cyg A without a stellar H-wall absorption component, but this fit required a stellar  $\text{Ly}\alpha$  line profile with a very deep self-reversal. Since we consider this profile to be unlikely, we also present a fit with a more reasonable model of the intrinsic stellar  $\text{Ly}\alpha$  line, which requires a stellar H-wall absorption component. The properties of this component are consistent with theoretical expectations, so we consider the second  $\text{Ly}\alpha$  fit to be the better interpretation of the data.

3. We were also able to fit the  $\text{Ly}\alpha$  line of 40 Eri A without a stellar H-wall component. This fit has a very low deuterium-to-hydrogen ratio,  $\text{D}/\text{H} = (1.11 \pm 0.09) \times 10^{-5}$ , whereas all previous LIC measurements are consistent with  $\text{D}/\text{H} \approx 1.5 \times 10^{-5}$ . If correct, this would be proof that  $\text{D}/\text{H}$  varies within the LIC, which would have important rami-

fications for cosmology and Galactic chemical evolution models. However, in a second fit to the data we were able to show that the expected  $\text{D}/\text{H} = 1.5 \times 10^{-5}$  result could be recovered simply by adding to the analysis a stellar H-wall component with reasonable attributes. Given the lack of corroborating evidence for a variable  $\text{D}/\text{H}$  ratio within the LIC, we consider this second fit to be the preferred interpretation of the data.

4. The temperatures ( $T$ ), nonthermal velocities ( $\xi$ ), and Mg depletions [ $D(\text{Mg})$ ] measured for the LIC toward 61 Cyg A and 40 Eri A are all consistent with previously published results (see Tables 3 and 4).

By compiling the properties of all stellar H walls detected to date (some of them only tentatively detected), we have explored several ways in which the measured H-wall properties can be used to study stellar winds and the LISM. Our findings are summarized as follows:

1. We find that H-wall temperatures increase with stellar velocity through the LISM in a manner consistent with the predictions of hydromagnetic shock jump conditions. The exact predictions are dependent on the hydrogen ionization fraction ( $x$ ) and the ratio of magnetic to thermal pressure in the LISM ( $\alpha$ ). While acknowledging the existence of several potentially important sources of systematic error, we tentatively find that  $x < 0.6$  and  $\alpha < 2$  based on comparing the data with the jump conditions. The latter upper limit implies an upper limit to the LISM magnetic field of  $B < 5 \mu\text{G}$ . Both upper limits combined suggest that the plasma Mach number of the interstellar wind flowing into the heliosphere is  $M_A > 1.3$ , meaning that the collision should be supersonic and that a bow shock must therefore exist outside the heliopause in the upwind direction.

2. Stellar H walls can be used as probes for ISM properties. For example, the mere existence of an H wall around 40 Eri A leads us to conclude that this star must be located within the LIC despite a low average H I density along this line of sight. This low average density must be due to either a decrease in total density from the Sun toward 40 Eri A or an increase in the hydrogen ionization fraction along the line of sight.

3. We estimate stellar wind pressures ( $P_{\text{wind}}$ ) from the H-wall column densities, and we try to correlate these pressures (evaluated at the stellar surfaces) with X-ray surface fluxes ( $F_X$ ). Our results appear to be consistent with a  $P_{\text{wind}} \propto F_X^{-1/2}$  relation that is also consistent with the variations of  $P_{\text{wind}}$  and  $F_X$  observed during the solar activity cycle. If this relation can in fact be applied to solar-like stars, one can study stellar wind properties simply by measuring stellar X-rays. One implication of this is that wind pressures and mass-loss rates are then predicted to increase with stellar age (see relations [13] and [14]).

We hope that this work will stimulate additional modeling of LISM/stellar wind interactions, particularly for stars other than the Sun, now that observations exist that are relevant to such models.

We would like to thank L. Williams and G. Zank for useful discussions regarding models of the heliosphere and the anonymous referee for several helpful suggestions. This work is supported by grant GO-06617.01-95A from the Space Telescope Science Institute to the University of Colorado and by NASA grant S-56460-D.

## REFERENCES

- Anders, E., & Grevesse, N. 1989, *Geochim. Cosmochim. Acta*, 53, 197
- Ayres, T. R. 1997, *J. Geophys. Res.*, 102, 1641
- Baliunas, S. L., et al. 1995, *ApJ*, 438, 269
- Baranov, V. B., & Malama, Y. G. 1993, *J. Geophys. Res.*, 98, 15157
- . 1995, *J. Geophys. Res.*, 100, 14755
- Beavers, W. I., & Eitter, J. J. 1986, *ApJS*, 62, 147
- Beuermann, K., Kanbach, G., & Berkhuijsen, E. M. 1985, *A&A*, 153, 17
- Bevington, P. R., & Robinson, D. K. 1992, *Data Reduction and Error Analysis for the Physical Sciences* (New York: McGraw-Hill)
- Bloemen, H. 1987, in *Interstellar Processes*, ed. D. H. Hollenbach & H. A. Thronson, Jr. (Dordrecht: Reidel), 143
- Brandt, J. C., et al. 1994, *PASP*, 106, 890
- Breig, E. L., Hanson, W. B., Hoffman, J. H., & Kayser, D. C. 1976, *J. Geophys. Res.*, 81, 2677
- Brekke, P., Kjeldseth-Moe, O., Bartoe, J.-D. F., & Brueckner, G. E. 1991, *ApJS*, 75, 1337
- Cox, D. P., & Reynolds, R. J. 1987, *ARA&A*, 25, 203
- Dempsey, R. C., Linsky, J. L., Fleming, T. A., & Schmitt, J. H. M. M. 1993, *ApJS*, 86, 599
- Dring, A. R., Murthy, J., Henry, R. C., Landsman, W., Audouze, J., Linsky, J., Moos, W., & Vidal-Madjar, A., Audouze, A., & Landsman, V. 1997, *ApJ*, 488, 760
- Frisch, P. C. 1993, *ApJ*, 407, 198
- Gayley, K. G., Zank, G. P., Pauls, H. L., Frisch, P. C., & Welty, D. E. 1997, *ApJ*, 487, 259
- Gilliland, R. L. 1994, *GHRs Instrument Science Report 063* (Baltimore: Space Telescope Science Institute)
- Gliese, W., & Jahreiss, H. 1991, *Third Catalogue of Nearby Stars* (Heidelberg: Astronomischen Rechen-Institut)
- Gry, C., Lemonon, L., Vidal-Madjar, A., Lemoine, M., & Ferlet, R. 1995, *A&A*, 302, 497
- Heap, S. R., et al. 1995, *PASP*, 107, 871
- Hedin, A. E. 1983, *J. Geophys. Res.*, 88, 10,170
- Heiles, C. 1987, in *Interstellar Processes*, ed. D. H. Hollenbach & H. A. Thronson, Jr. (Dordrecht: Reidel), 171
- Hinteregger, H. E. 1981, *Adv. Space Res.*, 1, 39
- Hirshfeld, A., Sinnott, R. W., & Ochsenbein, R. 1991, *Sky Catalogue 2000.0*, Vol. 1 (Cambridge: Cambridge Univ. Press)
- Holzer, T. E. 1972, *J. Geophys. Res.*, 77, 5407
- . E. 1989, *ARA&A*, 27, 199
- Ip, W.-H., & Axford, W. I. 1985, *A&A*, 149, 7
- Kass, D. H., & Yung, Y. L. 1995, *Science*, 268, 697
- Krishnamurthi, A., Pinsonneault, M. H., Barnes, S., & Sofia, S. 1997, *ApJ*, 480, 303
- Lallement, R., Bertin, P., Ferlet, R., Vidal-Madjar, A., & Bertaux, J. L. 1994, *A&A*, 286, 898
- Lallement, R., Ferlet, R., Lagrange, A. M., Lemoine, M., & Vidal-Madjar, A. 1995, *A&A*, 304, 461
- Lazarus, A. J., & McNutt, R. L., Jr. 1990, in *Physics of the Outer Heliosphere*, ed. S. Grzedzielski & D. E. Page (New York: Pergamon), 229
- Lee, M. A. 1996, in *The Heliosphere in the Local Interstellar Medium*, ed. R. von Steiger, R. Lallement, & M. A. Lee (Dordrecht: Kluwer), 109
- Linsky, J. L., et al. 1993, *ApJ*, 402, 694
- Linsky, J. L., Diplas, A., Wood, B. E., Brown, A., Ayres, T. R., & Savage, B. D. 1995, *ApJ*, 451, 335
- Linsky, J. L., & Wood, B. E. 1996, *ApJ*, 463, 254
- . 1997, in *Primordial Nuclei and their Galactic Evolution*, ed. N. Prantzos, M. Tosi, & R. von Steiger (Dordrecht: Kluwer), in press
- Luhmann, J. G., & Bauer, S. J. 1992, in *Venus and Mars: Atmospheres, Ionospheres, and Solar Wind Interactions*, ed. J. G. Luhmann, M. Tatrallyay, & R. O. Pepin (Washington: AGU), 417
- Parker, E. N. 1963, *Interplanetary Dynamical Processes*, (New York: Wiley-Interscience)
- Pauls, H. L., Zank, G. P., & Williams, L. L. 1995, *J. Geophys. Res.*, 100, 21,595
- Phillips, S., Kearsley, S., Osborne, J. L., Haslam, C. G. T., & Stoffel, H. 1981a, *A&A*, 98, 286
- . 1981b, *A&A*, 103, 405
- Piskunov, N., Wood, B. E., Linsky, J. L., Dempsey, R. C., & Ayres, T. R. 1997, *ApJ*, 474, 315
- Rand, R. J., & Kulkarni, S. R. 1989, *ApJ*, 343, 760
- Robinson, R. D., Blackwell, J., Feggans, K., Lindler, D., Norman, D., & Shore, S. N. 1992, *A User's Guide to the GHRs Software*, Version 2.0 (Greenbelt, MD: Goddard Space Flight Center)
- Schmitt, J. H. M. M., Fleming, T. A., & Giampapa, M. S. 1995, *ApJ*, 450, 401
- Shu, F. H. 1992, *The Physics of Astrophysics*, Vol. 2 (Mill Valley: Univ. Science Books)
- Wallis, M. 1975, *Nature*, 254, 207
- Williams, L. L., Hall, D. T., Pauls, H. L., & Zank, G. P. 1997, *ApJ*, 476, 366
- Wood, B. E. 1996, Ph.D. thesis, University of Colorado
- Wood, B. E., Alexander, W. R., & Linsky, J. L. 1996, *ApJ*, 470, 1157
- Wood, B. E., & Linsky, J. L. 1997, *ApJ*, 474, L39
- Wood, B. E., Linsky, J. L., & Ayres, T. R. 1997, *ApJ*, 478, 745
- Zank, G. P., Pauls, H. L., Williams, L. L., & Hall, D. T. 1996, *J. Geophys. Res.*, 101, 21,639